REPORT DOCUMENTATION PAGE

Form Approved OMB NO. 0704-0188

1. REPORT DATE (DD-MM-YYYY)	2. REPORT TYPE	3. DATES COVERED (From - To)
22-04-2022	Final Report	26-Feb-2019 - 25-Feb-2022

4. TITLE AND SUBTITLE
Final Report: Phononic Effects in Diamond Electronics

5a. CONTRACT NUMBER
W911NF-19-2-0086

5b. GRANT NUMBER

5c. PROGRAM ELEMENT NUMBER
111111

6. AUTHORS

5d. PROJECT NUMBER

5e. TASK NUMBER

5f. WORK UNIT NUMBER

7. PERFORMING ORGANIZATION NAMES AND ADDRESSES
University of Illinois - Chicago
809 South Marshfield Avenue
MB 502, M/C 551
Chicago, IL 60612 -4305

8. PERFORMING ORGANIZATION REPORT NUMBER

9. SPONSORING/MONITORING AGENCY NAME(S) AND ADDRESS (ES)
U.S. Army Research Office
P.O. Box 12211
Research Triangle Park, NC 27709-2211

10. SPONSOR/MONITOR'S ACRONYM(S)
ARO

11. SPONSOR/MONITOR'S REPORT NUMBER(S)
74793-EL-H.5

12. DISTRIBUTION AVAILIBILITY STATEMENT
Approved for public release; distribution is unlimited.

13. SUPPLEMENTARY NOTES
The views, opinions and/or findings contained in this report are those of the author(s) and should not contrued as an official Department of the Army position, policy or decision, unless so designated by other documentation.

14. ABSTRACT

15. SUBJECT TERMS

16. SECURITY CLASSIFICATION OF:			17. LIMITATION OF ABSTRACT	15. NUMBER OF PAGES	19a. NAME OF RESPONSIBLE PERSON
a. REPORT	b. ABSTRACT	c. THIS PAGE			Mitra Dutta
UU	UU	UU	UU		19b. TELEPHONE NUMBER 312-355-3221

RPPR Final Report
as of 26-Apr-2022

Agency Code: 21XD

Proposal Number: 74793ELH **Agreement Number: W911NF-19-2-0086**
INVESTIGATOR(S):

Name: Mitra Dutta Ph.D
Email: dutta@uic.edu
Phone Number: 3123553221
Principal: Y

Organization: **University of Illinois - Chicago**
Address: 809 South Marshfield Avenue, Chicago, IL 606124305
Country: USA
DUNS Number: 098987217 EIN: 376000511

Report Date: 25-May-2022 Date Received: 22-Apr-2022
Final Report for Period Beginning 26-Feb-2019 and Ending 25-Feb-2022
Title: Phononic Effects in Diamond Electronics
Begin Performance Period: 26-Feb-2019 **End Performance Period:** 25-Feb-2022
Report Term: 0-Other

Submitted By: Mitra Dutta Email: dutta@uic.edu
Phone: (312) 355-3221

STEM Degrees: 2 **STEM Participants:** 3

Major Goals: : The goal of this effort with Army Research Laboratory was to overcome some of the limitations in the development of diamond-based nanoelectronic components associated with stable doping, defects and fabrication issues and lower carrier mobility. The theoretical effort focuses on understanding the effects of 2D phonons both optical and acoustic phonon scattering is modified because the carriers in these transistors are 2D holes produced by surface transfer doping. During the period of the grant the theoretical thrust of this effort has been on the formulation of the effects of the remote polar phonons and the contribution of the effects of the surface acoustic phonons on the scattering rates and thus on the mobility of these transistors. In parallel we are also fabricating the devices experimentally and discussing and comparing these fabricated devices with the ones that are being fabricated at ARL After the end of the second year, there was no further funding unfortunately due to cuts at ARL. However the grant has inspired a search for better materials systems for the capping layer for lower phonon scattering and thus higher mobilities and work on c-BN as the surface layer was completed and published before the end of the grant. In addition we also looked at fabrication of liquid ion gate transistors in collaboration with Argonne National Lab and that work too was published during the period of the grant.

Accomplishments: During this period of the grant we completed and reported on a number of significant contributions to the theoretical efforts proposed. We completed and published an evaluation of the scattering rates of holes by remote-IF-polar phonons in the diamond structure is formulated for the first time, and in additional the effect of surface acoustic phonons on mobilities in diamond with 2D holes and in c-BN compared the effects of the two scattering mechanisms, These results show that hole scattering from remote polar phonons can dominate over other hole-phonon scattering mechanism by seven or more orders of magnitude; thus, while the use of polar overlayers may contribute to desired doping effects, there is a substantial penalty associated with hole remote-polar-phonon scattering. This model adopted in the case of remote-IF-polar phonons is suitable to describe several promising polar materials, such as AlN, w-BN and c-BN. The remote polar phonon scattering work has been written up and published in Diamond and Related Materials, Vol 101 (2020) 107650. G. Bonomo, A Mohamed, S. Farid, K. Park, M. Dutta and M.A Stroscio. “Contribution of remote interface polar phonons in the hole mobility of diamond”. It has also been presented at the WOCSEMMAD conference at Palm Springs, CA in Feb 2020.
We then studied a similar approach to study the effects of surface-acoustic phonon scattering on the charge transport behavior of diamond based FET devices. This work focused on detailed formulation of relaxation times due to the hole-surface-acoustic phonon scattering, which appears to have been an overlooked scattering mechanism important to diamond-based devices. The matrix element, scattering rates and relaxation times have been calculated by taking into account, for the first time Rayleigh waves near the surface. This is achieved by quantizing the Rayleigh waves and using the corresponding acoustic phonon to calculate the Fermi golden rule based scattering rate of holes in the two-dimensional hole gas. The results show that the scattering of holes with

surface acoustic Rayleigh waves reduced relative to scattering from bulk 3D acoustic phonons. Moreover, the mobilities are found to be higher than those based on the theory for 3D acoustic phonons. The results reveal significant insights to diamond based electronics having acoustic phonons Rayleigh waves thus opening new research endeavors. This was submitted and has been published in Carbon, Vol 169, Pages 488 -500, "Surface acoustics phonon scattering in 2D-hole gas of diamond based FET devices, " Ramji Singh, Giorgio Bonomo, Sidra Farid, Mahesh R. Neupane,. Glen Birdwell, Tony G. Ivanov, Mitra Dutta, Michael A.Stroscio.
We then looked at the effect of c-BN layer on top of the diamond and investigating the effect that the overlayer has on the mobility compared to the previous efforts. We investigates phonon-dominated mobilities for carriers in a diamond field effect transistor with a cubic Boron Nitride (cBN) overlayer. We investigate the intra-subband scattering due to interaction of electrons with acoustic phonons, treated properly as quantized surface acoustic Rayleigh waves, and include, for the first time, the interaction with remote polar phonons originating in the cBN overlayer. We concluded that the surface acoustic phonon scattering is the dominant mechanism limiting the mobility of electrons for temperatures below 375 K. This was published in IEEE Electron Device Letters “Phonon-Dominated Mobilities for Carriers in a Diamond Field Effect Transistor With a cBN Overlayer” Ramji Singh, Michael A. Stroscio, and Mitra Dutta.
We also performed some experimental work on fabricating Diamond transistors with hole gas and liquid ion gate and were able to demonstrate fairly high mobilities with there. These results were published in Nanotechnology. B. Hsu, S Farid, J Averion-Puttrich, AV Sumant, MA Stroscio, M Dutta, ‘High performance ionic-liquid-gated air doped diamond field-effect transistors’ Nanotechnology 32 (13), 135205.

Training Opportunities: During the period of the grant, Giordio Bonomo received his MS degree and left to pursue his PhD in Italy, Ahmed Mohamed graduated with a PhD and accepted a postdoc at University of Pennsylvania, Willilam Troy worked briefly on this project before working a different project and has since graduated.with a PhD and Ramji Singh is close ot receiving his PhD. Two postdocs, Bo Hsu and Sidra Farid, were also involved, mainly in the experimental portion of the grant and worked with Argonne National Laboratory.

Results Dissemination: Regular meetings were held with ARL scientists during the period of the grant. These were every two weeks with Glen Birdwell and with Mahesh Neupane. After the pandemic started these were held monthly. In addition to the papers, the work was presented at WOCSEMMAD and also at the Diamond workshop organized by Michigan State University in October 2020.

Honors and Awards: Nothing to Report

Protocol Activity Status:

Technology Transfer: No patents though the interaction with DoD scientists was reported in Dissemination portion of the report.

PARTICIPANTS:

Participant Type: PD/PI
Participant: Mitra Dutta
Person Months Worked: 3.00 **Funding Support:**
Project Contribution:
National Academy Member: N

Participant Type: Co PD/PI
Participant: Michael A. Stroscio
Person Months Worked: 3.00 **Funding Support:**
Project Contribution:
National Academy Member: N

Participant Type: Graduate Student (research assistant)

RPPR Final Report
as of 26-Apr-2022

Participant: Giorgio Bonomo
Person Months Worked: 1.00 **Funding Support:**
Project Contribution:
National Academy Member: N

Participant Type: Graduate Student (research assistant)
Participant: Ramji Singh
Person Months Worked: 10.00 **Funding Support:**
Project Contribution:
National Academy Member: N

Participant Type: Graduate Student (research assistant)
Participant: Ahmed Mohamed
Person Months Worked: 4.00 **Funding Support:**
Project Contribution:
National Academy Member: N

ARTICLES:

Publication Type: Journal Article Peer Reviewed: Y **Publication Status:** 1-Published
Journal: Diamond and Related Materials
Publication Identifier Type: DOI Publication Identifier: https://doi.org/10.1016/j.diamond.2019.1076
Volume: 101 Issue: 9 First Page #: 107649
Date Submitted: 8/11/21 12:00AM Date Published: 9/11/20 7:47PM
Publication Location:
Article Title: Contribution of remote interface polar phonons in the hole mobility of diamond
Authors: Giorgio Bonomo, Ahmed Mohamed Sidra Farid, Kihoon Park, Mitra Dutta Michael A. Stroscio
Keywords: Diamond, Mobility, Phonons, Scattering mechanism FETs Heterostructures
Abstract: The role of remote interface polar phonon modes on the electronic transport properties of dimensionally confined diamond structures have been investigated in detail. By employing a dielectric continuum model, scattering rates, hole mobility and relaxation times in mesoscopic diamond-based devices are calculated. The performance has been analyzed by inserting polar over layers on diamond with wide-band gap materials such as AlNor w ? BN. We have shown that a Fröhlich potential due to the interface optical phonon modes in the upper layer is created, that decays into diamond resulting in the existence of a remote polar phonon potential in the material. Hole scattering from remote polar phonons dominate on the order of two or more in magnitude resulting in substantial decrease in hole mobility in diamond. Thus, the present research will provide a milestone for understanding interface phonons that penetrate to the two-dimensional hole gas (2DHG) in confined diamond structures as compared
Distribution Statement: 2-Distribution Limited to U.S. Government agencies only; report contains proprietary info
Acknowledged Federal Support: **Y**

RPPR Final Report
as of 26-Apr-2022

Publication Type: Journal Article Peer Reviewed: Y **Publication Status:** 1-Published
Journal: Carbon
Publication Identifier Type: DOI Publication Identifier: https://doi.org/10.1016/j.carbon.2020.07.078
Volume: 169 Issue: 11 First Page #: 488
Date Submitted: 8/11/21 12:00AM Date Published:
Publication Location:
Article Title: Surface-acoustics phonon scattering in 2D-hole gas of diamond based FET devices
Authors: Ramji Singh, Giorgio Bonomo , Sidra Farid, Mahesh R. Neupane, A. Glen Birdwell , Tony G. Ivanov , Mi
Keywords: Diamond Phonons Surface-acoustic phonons Scattering rates FETs Heterostructures
Abstract: We report on the effects of surface-acoustic phonon scattering on the charge transport behavior of diamond based FET devices. Motivated by the promising role of diamond in the realization of high power and high frequency electronic devices, the present work is focused on detailed formulation of relaxation times due to the hole-surface-acoustic phonon scattering, which appears to have been an overlooked scattering mechanism important to diamond-based devices. The matrix element, scattering rates and relaxation times have been calculated by taking into account, for the first time Rayleigh waves near the surface. This is achieved by quantizing the Rayleigh waves and using the corresponding acoustic phonon to calculate the Fermi golden rule based scattering rate of holes in the two-dimensional hole gas. The results show that the scattering of holes with surface acoustic Rayleigh waves reduced relative to scattering from bulk 3D acoustic phonons.
Distribution Statement: 2-Distribution Limited to U.S. Government agencies only; report contains proprietary info
Acknowledged Federal Support: **Y**

Publication Type: Journal Article Peer Reviewed: Y **Publication Status:** 1-Published
Journal: Nanotechnology
Publication Identifier Type: DOI Publication Identifier: https://doi.org/10.1016/j.diamond.2019.1076
Volume: 32 Issue: 4 First Page #: 135205
Date Submitted: 8/11/21 12:00AM Date Published: 8/12/21 1:10AM
Publication Location:
Article Title: High performance ionic-liquid-gated air doped diamond field-effect transistors
Authors: High performance ionic-liquid-gated air doped diamond field-effect transistors
Keywords: diamond, FET, ionic liquid, high power
Abstract: We report successful fabrication of high performance ion-gated field-effect transistors (FETs) on hydrogenated diamond surface. Investigations on the hydrogen (H)-terminated diamond by Hall effect measurements shows Hall mobility as high as ?200 cm2 V?1 s?1. In addition we demonstrate a rapid fabrication scheme for achieving stable high performance devices useful for determining optimal growth and fabrication conditions. We achieved H-termination using hydrogen plasma treatment with a sheet resistivity as low as ?1.3 k? /sq. Conductivity through the FET channel is studied as a function of bias voltage on the liquid ion-gated electrode from ?3.0 to 1.5 V. Stability of the H-terminated diamond surface was studied by varying the substrate temperature up to 350 °C. It was demonstrated that the sheet resistance and carrier densities remain stable over 3 weeks in ambient air atmosphere even at substrate temperatures up to 350 °C.
Distribution Statement: 2-Distribution Limited to U.S. Government agencies only; report contains proprietary info
Acknowledged Federal Support: **Y**

RPPR Final Report
as of 26-Apr-2022

Publication Type: Journal Article Peer Reviewed: Y **Publication Status:** 1-Published
Journal: IEEE Electron Device Letters
Publication Identifier Type: DOI Publication Identifier: Digital Object Identifier 10.1109/LED.2021.31
Volume: 43 Issue: 1 First Page #: 112
Date Submitted: 4/22/22 12:00AM Date Published: 1/22/22 6:37PM
Publication Location:
Article Title: Phonon-Dominated Mobilities for Carriers in a Diamond Field Effect Transistor With a cBN Overlayer
Authors: Ramji Singh , Michael A. Stroscio, Mitra Dutta,
Keywords: cBN, diamond, remote polar phonon, surface acoustic phonon, Rayleigh wave, scattering, FET.
Abstract: In this letter we investigate phonon-dominated mobilities for carriers in a diamond field effect transistor with a cubic Boron Nitride (cBN) overlayer. We investigate the intra-subband scattering due to interaction of electrons with acoustic phonons, treated properly as quantized sur┐face acoustic Rayleigh waves, and include, for the first time, the interaction with remote polar phonons originating in the cBN overlayer. We conclude that the surface acoustic phonon scattering is the dominant mechanism limiting the mobility of electrons for temperatures below 375 K.
Distribution Statement: 1-Approved for public release; distribution is unlimited.
Acknowledged Federal Support: **Y**

Partners

,

I certify that the information in the report is complete and accurate:
Signature: Mitra Dutta
Signature Date: 4/22/22 1:53PM

W911NF1920086 : Phononic Effects in Diamond Electronics

Reporting Period: FEB 26, 2019 to FEB 25, 2022

Date Received:

Submitter: Mitra Dutta

Major Goals

: The goal of this effort with Army Research Laboratory was to overcome some of the limitations in the development of diamond-based nanoelectronic components associated with stable doping, defects and fabrication issues and lower carrier mobility. The theoretical effort focuses on understanding the effects of 2D phonons both optical and acoustic phonon scattering is modified because the carriers in these transistors are 2D holes produced by surface transfer doping. During the period of the grant the theoretical thrust of this effort has been on the formulation of the effects of the remote polar phonons and the contribution of the effects of the surface acoustic phonons on the scattering rates and thus on the mobility of these transistors. In parallel we are also fabricating the devices experimentally and discussing and comparing these fabricated devices with the ones that are being fabricated at ARL After the end of the second year, there was no further funding unfortunately due to cuts at ARL. However the grant has inspired a search for better materials systems for the capping layer for lower phonon scattering and thus higher mobilities and work on c-BN as the surface layer was completed and published before the end of the grant. In addition we also looked at fabrication of liquid ion gate transistors in collaboration with Argonne National Lab and that work too was published during the period of the grant.

Accomplishments Under Goals

During this period of the grant we completed and reported on a number of significant contributions to the theoretical efforts proposed. We completed and published an evaluation of the scattering rates of holes by remote-IF-polar phonons in the diamond structure is formulated for the first time, and in additional the effect of surface acoustic phonons on mobilities in diamond with 2D holes and in c-BN compared the effects of the two scattering mechanisms, These results show that hole scattering from remote polar phonons can dominate over other hole-phonon scattering mechanism by seven or more orders of magnitude; thus, while the use of polar overlayers may contribute to desired doping effects, there is a substantial penalty associated with hole remote-polar-phonon scattering. This model adopted in the case of remote-IF-polar phonons is suitable to describe several promising polar materials, such as AlN, w-BN and c-BN. The remote polar phonon scattering work has been written up and published in Diamond and Related Materials, Vol 101 (2020) 107650. G. Bonomo, A Mohamed, S. Farid, K. Park, M. Dutta and M.A Stroscio. “Contribution of remote interface polar phonons in the hole mobility of diamond”. It has also been presented at the WOCSEMMAD conference at Palm Springs, CA in Feb 2020. We then studied a similar approach to study the effects of surface-acoustic phonon scattering on the charge transport behavior of diamond based FET devices. This work focused on detailed formulation of relaxation times due to the hole-surface-acoustic phonon scattering, which appears to have been an overlooked scattering mechanism important to diamond-based devices. The matrix element, scattering rates and relaxation times have been calculated by taking into account, for the first time Rayleigh waves near the surface. This is achieved by quantizing the Rayleigh waves and using the corresponding acoustic phonon to

calculate the Fermi golden rule based scattering rate of holes in the two-dimensional hole gas. The results show that the scattering of holes with surface acoustic Rayleigh waves reduced relative to scattering from bulk 3D acoustic phonons. Moreover, the mobilities are found to be higher than those based on the theory for 3D acoustic phonons. The results reveal significant insights to diamond based electronics having acoustic phonons Rayleigh waves thus opening new research endeavors. This was submitted and has been published in Carbon, Vol 169, Pages 488 -500, "Surface acoustics phonon scattering in 2D-hole gas of diamond based FET devices, " Ramji Singh, Giorgio Bonomo, Sidra Farid, Mahesh R. Neupane,. Glen Birdwell, Tony G. Ivanov, Mitra Dutta, Michael A.Stroscio. We then looked at the effect of c-BN layer on top of the diamond and investigating the effect that the overlayer has on the mobility compared to the previous efforts. We investigates phonon-dominated mobilities for carriers in a diamond field effect transistor with a cubic Boron Nitride (cBN) overlayer. We investigate the intra-subband scattering due to interaction of electrons with acoustic phonons, treated properly as quantized surface acoustic Rayleigh waves, and include, for the first time, the interaction with remote polar phonons originating in the cBN overlayer. We concluded that the surface acoustic phonon scattering is the dominant mechanism limiting the mobility of electrons for temperatures below 375 K. This was published in IEEE Electron Device Letters “Phonon-Dominated Mobilities for Carriers in a Diamond Field Effect Transistor With a cBN Overlayer” Ramji Singh, Michael A. Stroscio, and Mitra Dutta. We also performed some experimental work on fabricating Diamond transistors with hole gas and liquid ion gate and were able to demonstrate fairly high mobilities with there. These results were published in Nanotechnology. B. Hsu, S Farid, J Averion-Puttrich, AV Sumant, MA Stroscio, M Dutta, ‘High performance ionic-liquid-gated air doped diamond field-effect transistors’ Nanotechnology 32 (13), 135205.

Plans Next Period

Results Dissemination

Regular meetings were held with ARL scientists during the period of the grant. These were every two weeks with Glen Birdwell and with Mahesh Neupane. After the pandemic started these were held monthly. In addition to the papers, the work was presented at WOCSEMMAD and also at the Diamond workshop organized by Michigan State University in October 2020.

Honors and Awards

Nothing to Report

Training Opportunities

During the period of the grant, Giordio Bonomo received his MS degree and left to pursue his PhD in Italy, Ahmed Mohamed graduated with a PhD and accepted a postdoc at University of Pennsylvania, Willilam Troy worked briefly on this project before working a different project and has since graduated.with a PhD and Ramji Singh is close ot receiving his PhD. Two postdocs, Bo Hsu and Sidra Farid, were also involved, mainly in the experimental portion of the grant and worked with Argonne National Laboratory.

Technology Transfer

No patents though the interaction with DoD scientists was reported in Dissemination portion of the report.

Participants

Name	Role	Person Months
Stroscio, Michael	Co PD/PI	3
Bonomo, Giorgio	Graduate Student (research assistant)	1
Mohamed, Ahmed	Graduate Student (research assistant)	4
Singh, Ramji	Graduate Student (research assistant)	10
Dutta, Mitra	PD/PI	3

Diamond & Related Materials 101 (2020) 107650

Contents lists available at ScienceDirect

Diamond & Related Materials

journal homepage: www.elsevier.com/locate/diamond

Contribution of remote interface polar phonons in the hole mobility of diamond

Giorgio Bonomo[a], Ahmed Mohamed[b,*], Sidra Farid[b], Kihoon Park[c], Mitra Dutta[b], Michael A. Stroscio[b]

[a] Department of Information Technology and Electrical Engineering, ETH Zürich, Zürich CH-8092, Switzerland
[b] Department of Electrical and Computer Engineering, University of Illinois at Chicago, Chicago, IL 60607, USA
[c] Department of Electrical and Computer Engineering, University of Illinois at Urbana-Champaign, Urbana, IL 61801, USA

ARTICLE INFO

Keywords:
Diamond
Mobility
Phonons
Scattering mechanism
FETs
Heterostructures

ABSTRACT

The role of remote interface polar phonon modes on the electronic transport properties of dimensionally confined diamond structures have been investigated in detail. By employing a dielectric continuum model, scattering rates, hole mobility and relaxation times in mesoscopic diamond-based devices are calculated. The performance has been analyzed by inserting polar over layers on diamond with wide-band gap materials such as *AlN* or $w - BN$. We have shown that a Fröhlich potential due to the interface optical phonon modes in the upper layer is created, that decays into diamond resulting in the existence of a remote polar phonon potential in the material. Hole scattering from remote polar phonons dominate on the order of two or more in magnitude resulting in substantial decrease in hole mobility in diamond. Thus, the present research will provide a milestone for understanding interface phonons that penetrate to the two-dimensional hole gas (2DHG) in confined diamond structures as compared to their bulk counterpart and can also be applied to other polar materials used for doping.

1. Introduction

Charge carriers in 2D materials, diamond, graphene and carbon nanotubes can remotely couple to surface polar phonons (SPP) when brought in close proximity to a polar substrate via a mechanism usually known as remote interface phonon (RIP) scattering [1,2]. In this phenomenon, the remote coupling between charge carriers and surface polar phonons in the underlying polar substrates is facilitated by oscillating electric fields created by SPPs and accompanied by energy exchange and momentum. Because of the inelastic nature of SPPs, they also provide a pathway to saturation of current in conjunction with intrinsic optical phonons [3]. Indeed, remote interface phonons, such as Rayleigh waves, can penetrate (with an exponential fall-off) up to 10s of nanometers and thus plays a critical role on scales of 10 nm or even less.

Since the experimental realization of diamond devices owing to its outstanding properties including high breakdown field, thermal conductivity and high carrier mobility, next generation of outperforming nanoelectronic devices is predicted to be led by diamond implementation industry. The extremely high intrinsic carrier mobilities along with extra ordinary characteristics of diamond will naturally lead to its utilization in high speed transistors and radio frequency (RF) electronics. It is extremely critical for such high frequency devices to be able to accurately determine low-field mobility issues and scattering rates. The importance of RIPs have already been realized in other materials like graphene/SiO_2 devices (Ong et al; Koh et al.; Li et al.)) [4–6] and on Si/SiO_2 inversion layers (K. Hess et al.; B. T. Moore et al.) [7,8]. They have realized the importance of RIPs for graphene/SiO_2 devices where as Pernot et al. has discussed the Hall hole mobility of homo epitaxial boron-doped diamond taking into account only bulk acoustic phonons and nonpolar optical phonon modes [9]. Thus, all previous efforts on dimensionally confined diamond structures for the phononic effects are based on bulk phonons. To our knowledge, there has not been any efforts that consider interface phonon modes instead of bulk phonons, when calculating hole mobility values in both H-terminated diamond and diamond devices with other surface acceptor donors such as V_2O_5, MoO_3, WO_3 or AlN.

These interface phonons in diamond devices penetrate to the two-dimensional hole gas (2DHG) which is located only a few nanometers from the diamond surface exhibiting p-type conductivity. Researchers have provided a good starting point in the comprehension of the mechanisms leading to the formation of a high mobility 2DHG under the

* Corresponding author.
E-mail address: amoham55@uic.edu (A. Mohamed).

https://doi.org/10.1016/j.diamond.2019.107650
Received 23 September 2019; Received in revised form 5 November 2019; Accepted 26 November 2019
Available online 11 December 2019
0925-9635/

surface of H-terminated diamond [10]. It is found that the presence of H-terminated diamond is one necessary requirement for the appearance of the surface conductivity as exposure to atmospheric agents is essential to provide a water layer on the surface of diamond, necessary for the creation of the 2DHG. Further research demonstrated the possibility of exploiting transition metal-oxides characterized by a high electron affinity material such as vanadium oxide V_2O_5 [11] or molybdenum trioxide MoO_3 [12] to induce surface transfer doping. This is done to improve the thermal stability and carrier concentration in respect to the doping obtained by atmospheric adsorbates. A serious limitation to the 2DHG is its propensity to degradation when prone to higher temperatures or stability over time. To overcome this problem, a passivation layer of *AlN*, Al_2O_3 or *BN* are proposed by researchers as exploitable polar materials in order to encapsulate the 2DHG. Other solutions contemplate the insertion of oxygen-terminated diamond, characterized by a highly insulated surface, able to provide the required passivation.

The aim of this work reveals a detailed study and formulation of the contribution of hole–remote interface polar phonon interaction mechanism. We have also taken into account the insertion of a polar material on top of the diamond substrate; which is often neglected during the study of the mobility in diamond-based devices in order to understand its effectiveness and importance in depth. In order to describe the mechanism, we exploit the dielectric continuum model in our research [13]. This model is based on the idea that lattice vibrations give rise to an electrostatic polarization that can be described through the classical equations of electrostatics and is used to model remote interface polar phonons. Therefore, we have formulated the interaction Hamiltonian, and calculated the scattering rates through the Fermi Golden Rule approximation. By the mathematical formulation of the mechanism, its contribution is finally taken into account, in an effort to obtain a complete picture of the phenomena determining the mobility inside dimensionally confined nanoscale diamond-based devices and giving new guidelines for their development.

This paper is organized as follows: In Section 2 we specify the model system and develop formulism for optical phonon interaction Hamiltonian and introduced Fang-Howard wavefunction to describe 2DHG at the surface vicinity and inserted polar over layers. Section 3 describes the scattering rates and matrix element predicted by the Fermi Golden rule for the proposed structure. Section 4 presents parameters and constants utilized for characterizing the remote interface optical phonon modes for the electron-phonon interaction Hamiltonian along with a quantitative analysis of scattering rates and mobilities from proposed heterostructures with polar over layers. Section 5 shows the conclusions whereas derived expressions and auxiliary formulas for the integrals used can be found in Appendixes A and B.

2. Hole-optical-phonon interaction Hamiltonian model

The investigation is carried out to study the leakage of remote polar phonons from the polar over layer into the diamond substrate. A polar layer is inserted as a passivation layer or for the realization of the gate dielectric that generates an evanescent interface phonon mode that decays into the diamond. In particular, structures exploiting *AlN* and $w-BN$ as layer materials are under investigation in this work, due to their advanced physical and electrical properties such as wide bandgap and high breakdown voltage that makes them promising choices for the realization of diamond-based FETs. Herein, the remote polar phonons originating from *AlN* (or $w-BN$) are remodeled assuming a high-quality surface of the material at the interface with diamond as shown in Fig. 1. The *c*-axis of the upper layer material is assumed to be perpendicular to the diamond surface, consistent with what was reported in Imura et al. [14], where the authors have discussed the growth of *AlN* on diamond for the fabrication of h-FETs.

The Hamiltonian obtained for proposed structure is derived from the Fröhlich interaction Hamiltonian in a wurtzite structure with two heterointerfaces and proper modifications related to the insertion of vacuum as external material with correct positioning of the axis [15].

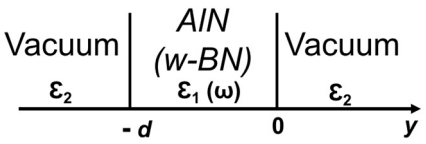

Fig. 1. Schematic drawing of double heterointerface system composed of polar overlay (*AlN* or w-*BN*) of width *d* and vacuum systems for evaluation of the IF phonon potential.

In such a structure, two possible solutions arise for the electrostatic potential, generally called symmetric and antisymmetric modes according to the symmetry/asymmetry of the potential in respect to a reference plane placed in the middle of the structure.

For the symmetric mode, it holds:

$$H_{IF}^{S} = \sum_{\mathbf{q}} \left[\frac{4\pi e_h^2 \hbar S^{-1}}{\left| (\partial/\partial\omega)\left(\sqrt{\epsilon_{\perp,1}\epsilon_{y,1}}\tanh\left(\sqrt{\epsilon_{\perp,1}/\epsilon_{y,1}}qd/2\right)-\epsilon_0\right)\right|} \right]^{\frac{1}{2}} \times \frac{1}{\sqrt{2q}} e^{i\mathbf{q}\cdot\mathbf{p}} \left(a_{\mathbf{q}} + a_{-\mathbf{q}}^{\dagger}\right) \times \begin{cases} e^{q(y+d)} & y < -d \\ \frac{\cosh\left(\sqrt{\epsilon_{\perp,1}/\epsilon_{y,1}}q(y+d/2)\right)}{\cosh\left(\sqrt{\epsilon_{\perp,1}/\epsilon_{y,1}}qd/2\right)} & -d \le y \le 0 \\ e^{-qy} & y > 0 \end{cases} \tag{1}$$

where the frequency ω is obtained by solving $\sqrt{\epsilon_{\perp,1}\epsilon_{y,1}}\tanh(\sqrt{\epsilon_{\perp,1}/\epsilon_{y,1}}qd/2) - \epsilon_0 = 0$, within the ranges determined by the conditions $\epsilon_{y,1}\epsilon_{y,2} < 0$ and $\epsilon_{y,1}\epsilon_{\perp,1} > 0$, ϵ_0 represents the vacuum permittivity and S represents the cross-sectional area of the sample. For the antisymmetric mode, it holds:

$$H_{IF}^{A} = \sum_{\mathbf{q}} \left[\frac{4\pi e_h^2 \hbar S^{-1}}{\left| (\partial/\partial\omega)\left(\sqrt{\epsilon_{\perp,1}\epsilon_{y,1}}\coth\left(\sqrt{\epsilon_{\perp,1}/\epsilon_{y,1}}qd/2\right)-\epsilon_0\right)\right|} \right]^{\frac{1}{2}} \times \frac{1}{\sqrt{2q}} e^{i\mathbf{q}\cdot\mathbf{p}} \left(a_{\mathbf{q}} + a_{-\mathbf{q}}^{\dagger}\right) \times \begin{cases} -e^{q(y+d)} & y < -d \\ \frac{\sinh\left(\sqrt{\epsilon_{\perp,1}/\epsilon_{y,1}}q(y+d/2)\right)}{\sinh\left(\sqrt{\epsilon_{\perp,1}/\epsilon_{y,1}}qd/2\right)} & -d \le y \le 0 \\ e^{-qy} & y > 0 \end{cases} \tag{2}$$

and the frequency ω is extracted by solving $\sqrt{\epsilon_{\perp,1}\epsilon_{y,1}}\coth(\sqrt{\epsilon_{\perp,1}/\epsilon_{y,1}}qd/2) - \epsilon_0 = 0$.

The dispersion relation for both the symmetric and antisymmetric modes types of IF phonon modes are depicted in Fig. 2.

The Howard-Fang wave function, used to describe the 2DHG is:

$$\Psi(\boldsymbol{r}) = |k\rangle = \sqrt{\frac{b^3}{2}}(y-l)\,e^{-\frac{1}{2}b\,(y-l)}\frac{e^{i\mathbf{k}_{\parallel}\mathbf{p}}}{\sqrt{S}},\ y-l>0 \tag{3}$$

with l representing the distance of the 2DHG from the surface, $\mathbf{k}_{\parallel} = (k_x, k_z)$, $\mathbf{p} = (x, z)$ and b is a variational parameter determined by minimizing the total energy of the system [16,17];

$$b = \left(\frac{33 m^* e_h^2 N_h}{8\epsilon_0\epsilon_r\hbar^2}\right)^{\frac{1}{3}} \tag{4}$$

with e_h representing the positive hole charge and N_h representing the 2DHG sheet density.

Fig. 3 illustrates the Fang-Howard wavefunction, while Fig. 4

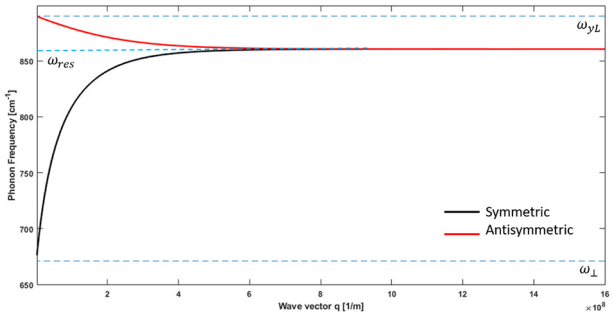

Fig. 2. Dispersion Relation for symmetric and antisymmetric IF modes in *AlN* (5 nm thickness), where ω_{res} represents the symmetric and antisymmetric resonance frequency, ω_{yL} is the longitudinal-optical phonon frequency and $\omega_{\perp}$ is the lattice dispersion frequency.

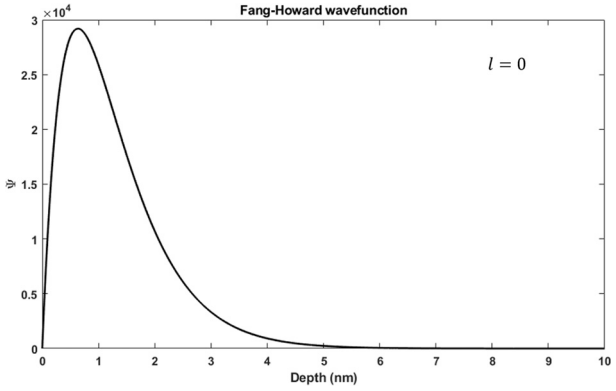

Fig. 3. Fang-Howard wavefunction of AlN-diamond structure under investigation.

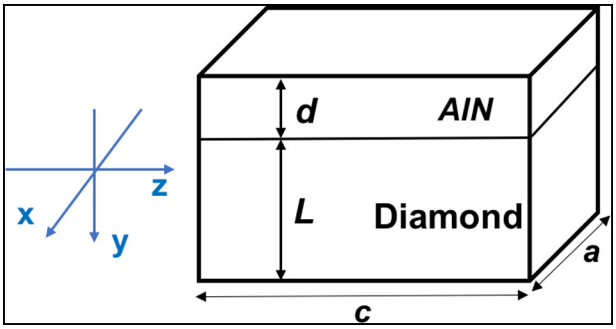

Fig. 4. Schematic representation for *AlN*-diamond structure under investigation.

illustrates the overall structure under analysis.

It is important to emphasize that when the exponentially decaying tail of the electrostatic potential Φ(r) reaches the diamond substrate, it is subject to a screening effect, leading to,

$$\Phi_d(\boldsymbol{r}) = \frac{\Phi(\boldsymbol{r})}{\epsilon_d}, \quad y > 0 \tag{5}$$

Finally, considering the leakage of the exponentially decaying tail of the electrostatic potential due to the polar layer on the diamond substrate (y > 0):

$$H_{IF}^{S} = \sum_q \left[\frac{2\pi e_h^2 \hbar (Sq\epsilon_d^2)^{-1}}{|(\partial/\partial\omega)(\sqrt{\epsilon_{\perp,1}\epsilon_{y,1}}\tanh(\sqrt{\epsilon_{\perp,1}/\epsilon_{y,1}}qd/2)-\epsilon_0)|}\right]^{\frac{1}{2}} \times e^{-qy}\left(a_q e^{iq\cdot\rho} - a_q^{\dagger} e^{-iq\cdot\rho}\right) \tag{6}$$

$$H_{IF}^{A} = \sum_q \left[\frac{2\pi e_h^2 \hbar (Sq\epsilon_d^2)^{-1}}{|(\partial/\partial\omega)(\sqrt{\epsilon_{\perp,1}\epsilon_{y,1}}\coth(\sqrt{\epsilon_{\perp,1}/\epsilon_{y,1}}qd/2)-\epsilon_0)|}\right]^{\frac{1}{2}} \times e^{-qy}\left(a_q e^{iq\cdot\rho} - a_q^{\dagger} e^{-iq\cdot\rho}\right) \tag{7}$$

3. Matrix element and scattering rate

The matrix element $M^{e,a}(q)$ for the symmetric case is formulated as,

$$M^{\{e,a\}}(q) = \left\langle \boldsymbol{k}', N_n + \frac{1}{2} \pm \frac{1}{2} \left| H_{def} \right| \boldsymbol{k}, N_n + \frac{1}{2} \mp \frac{1}{2} \right\rangle = \left[\frac{2\pi e_h^2 \hbar (Sq\epsilon_d^2)^{-1}}{|(\partial/\partial\omega)(\sqrt{\epsilon_{\perp,1}\epsilon_{y,1}}\tanh(\sqrt{\epsilon_{\perp,1}/\epsilon_{y,1}}qd/2)-\epsilon_0)|}\right]^{\frac{1}{2}} \times \langle \boldsymbol{k}' \left| e^{\mp i\boldsymbol{q}\boldsymbol{\rho}} e^{-qy} \right| \boldsymbol{k}\rangle (\mp)\left(n + \frac{1}{2} \pm \frac{1}{2}\right)^{\frac{1}{2}} \tag{8}$$

while for the antisymmetric case,

$$M^{\{e,a\}}(q) = \left\langle \boldsymbol{k}', N_n + \frac{1}{2} \pm \frac{1}{2} \left| H_{def} \right| \boldsymbol{k}, N_n + \frac{1}{2} \mp \frac{1}{2} \right\rangle = \left[\frac{2\pi e_h^2 \hbar (Sq\epsilon_d^2)^{-1}}{|(\partial/\partial\omega)(\sqrt{\epsilon_{\perp,1}\epsilon_{y,1}}\coth(\sqrt{\epsilon_{\perp,1}/\epsilon_{y,1}}qd/2)-\epsilon_0)|}\right]^{\frac{1}{2}} \times \langle \boldsymbol{k}' \left| e^{\mp i\boldsymbol{q}\boldsymbol{\rho}} e^{-qy} \right| \boldsymbol{k}\rangle (\mp)\left(n + \frac{1}{2} \pm \frac{1}{2}\right)^{\frac{1}{2}} \tag{9}$$

Using $H_{IF,\,D}$ as given by (6) and (7), one has for the overlap integral,

$$\langle \boldsymbol{k}' \left| e^{\mp i\boldsymbol{q}\boldsymbol{\rho}} e^{-qy} \right| \boldsymbol{k}\rangle = F(q)\delta_{\boldsymbol{k}'\|-\boldsymbol{k}\|\pm\boldsymbol{q}} \tag{10}$$

where the mathematical steps required and the final symbolic expression for F(q) are provided in Appendix A. Thus, the matrix element for the symmetric case is

$$M^{\{e,a\}}(q) = \left[\frac{2\pi e_h^2 \hbar (Sq\epsilon_d^2)^{-1}}{|(\partial/\partial\omega)(\sqrt{\epsilon_{\perp,1}\epsilon_{y,1}}\tanh(\sqrt{\epsilon_{\perp,1}/\epsilon_{y,1}}qd/2)-\epsilon_0)|}\right]^{\frac{1}{2}} F(q)(\mp)\left(n + \frac{1}{2} \pm \frac{1}{2}\right)^{\frac{1}{2}} \delta_{\boldsymbol{k}'\|-\boldsymbol{k}\|\pm\boldsymbol{q}} \tag{11}$$

while for the antisymmetric case it is,

$$M^{\{e,a\}}(q) = \left[\frac{2\pi e_h^2 \hbar (Sq\epsilon_d^2)^{-1}}{|(\partial/\partial\omega)(\sqrt{\epsilon_{\perp,1}\epsilon_{y,1}}\coth(\sqrt{\epsilon_{\perp,1}/\epsilon_{y,1}}qd/2)-\epsilon_0)|}\right]^{\frac{1}{2}} F(q)(\mp)\left(n + \frac{1}{2} \pm \frac{1}{2}\right)^{\frac{1}{2}} \delta_{\boldsymbol{k}'\|-\boldsymbol{k}\|\pm\boldsymbol{q}} \tag{12}$$

where the upper sign (+) corresponds to phonon emission and the lower sign (−) to absorption. It follows that:

$$|M^{\{e,a\}}(q)|^2 = |C|^2 F^2 \left(n + \frac{1}{2} \pm \frac{1}{2}\right)\delta_{\boldsymbol{k}'\|-\boldsymbol{k}\|\pm\boldsymbol{q}} \tag{13}$$

where C is a variable introduced for simplicity, represented for the symmetric as,

$$C = \left[\frac{2\pi e_h^2 \hbar (Sq\epsilon_d^2)^{-1}}{|(\partial/\partial\omega)(\sqrt{\epsilon_{\perp,1}\epsilon_{y,1}}\tanh(\sqrt{\epsilon_{\perp,1}/\epsilon_{y,1}}qd/2)-\epsilon_0)|}\right]^{\frac{1}{2}} \tag{14}$$

while for the antisymmetric case,

$$C = \left[\frac{2\pi e_h^2 \hbar (Sq\epsilon_d^2)^{-1}}{|(\partial/\partial\omega)(\sqrt{\epsilon_{\perp,1}\epsilon_{y,1}}\coth(\sqrt{\epsilon_{\perp,1}/\epsilon_{y,1}}qd/2)-\epsilon_0)|}\right]^{\frac{1}{2}} \tag{15}$$

Therefore, the total scattering rate (1/τ) predicted by the Fermi Golden Rule is given by:

$$\begin{aligned}\frac{1}{\tau} &= \frac{S}{(2\pi)^2}\int d^2\boldsymbol{q}\frac{2\pi}{\hbar}|C|^2F^2\left(n + \frac{1}{2} \pm \frac{1}{2}\right)\delta_{\boldsymbol{k}'\|-\boldsymbol{k}\|\pm\boldsymbol{q}}\delta \\ &\quad (E(\boldsymbol{k}') - E(\boldsymbol{k}) \pm \hbar\omega_q) \\ &= \frac{S}{2\pi\hbar}\int d^2\boldsymbol{q}\,|C|^2F^2\left(n + \frac{1}{2} \pm \frac{1}{2}\right)\delta_{\boldsymbol{k}'\|-\boldsymbol{k}\|\pm\boldsymbol{q}}\delta(E(\boldsymbol{k}') - E(\boldsymbol{k}) \pm \hbar\omega_q) \\ &= \frac{e_h^2}{\epsilon_r^2}\int d^2\boldsymbol{q}\frac{D(q,\omega)}{q}\left(n + \frac{1}{2} \pm \frac{1}{2}\right)\delta_{\boldsymbol{k}'\|-\boldsymbol{k}\|\pm\boldsymbol{q}}\delta(E(\boldsymbol{k}') - E(\boldsymbol{k}) \pm \hbar\omega_q)\end{aligned} \tag{16}$$

where the term $D(q,\omega)$ variable for the symmetric case is,

$$D(q,\omega) = \frac{F^2}{|(\partial/\partial\omega)(\sqrt{\epsilon_{\perp,1}\epsilon_{y,1}}\tanh(\sqrt{\epsilon_{\perp,1}/\epsilon_{y,1}}qd/2)-\epsilon_0)|} \tag{17}$$

In order to obtain the total contribution of both the symmetric and antisymmetric solutions, the two terms are eventually summed exploiting Matthiessen Rule:

$$\frac{1}{\tau} = \frac{1}{\tau_s} + \frac{1}{\tau_a} \tag{18}$$

As shown in Fig. 2, a strong relationship between the phonon wavenumber and frequency exists, that has to be taken into account explicitly when deriving the scattering rate through the Fermi Golden Rule. For this reason, a set of transformation analogous to the one reported in [18] is applied to the formulation obtained in Eq. (16). Considering $P(q,\omega) = e_h^2/\epsilon_r^2 D(q,\omega)\left(n + \frac{1}{2} \pm \frac{1}{2}\right)$ and $L(q,\omega,\theta) = E_{\mathbf{k}\mp\mathbf{q}} - E_{\mathbf{k}} \pm \hbar\omega$, it holds:

$$\frac{1}{\tau} = \int \frac{P}{q}\delta(L)d\boldsymbol{q} = \int P\delta(L)dq\,d\theta = \int P\left|\frac{dL}{dq}\right|^{-1} d\theta$$
$$= \int P\left|\frac{dL}{dq}\right|^{-1}\left|\frac{d\theta}{d\omega}\right| d\omega \tag{19}$$

The details of the transformation are provided in Appendix B. Therefore, the final formulation obtained is:

$$\frac{1}{\tau_a^e} = \mp\frac{m^* e_h^2}{\epsilon_r^2\hbar^2}\int_{\omega_1}^{\omega_2} \frac{\left(n + \frac{1}{2} \pm \frac{1}{2}\right)D(q,\omega)\sigma\left[\left(\frac{V_p}{q} \mp \frac{\hbar}{2m^*}\right)\frac{1}{V_g} - \frac{1}{q}\right]}{\left[\frac{q}{2} \mp \frac{m^*}{\hbar}(V_p - V_g)\right]\sqrt{\frac{1}{m^*}\left(2E_k - \frac{E_q}{2} \mp \hbar\omega\right) - V_p^2}} d\omega \tag{20}$$

$$\sigma = \begin{cases} 0 & if\ \frac{1}{m^*}\left(2E_k - \frac{E_q}{2} \mp \hbar\omega\right) - V_p^2 < 0 \\ 1\ otherwise \end{cases} \tag{21}$$

where the conditional variable σ is introduced to ensure energy and momentum conservation in accordance to Ref. 19, and the range $[\omega_1, \omega_2]$ is determined by the region of existence of the IF modes depicted in Fig. 2.

4. Numerical results and discussions

The numerical results obtained for the formulation of the scattering rate for remote IF optical phonons as calculated in Eq. (20) are presented in this section. The values of the numerical constants exploited for calculations are provided in Tables 1 and 2.

A MATLAB code based on the one developed by Mohamed et al. [23] is realized for the purpose of performing the numerical integration: the built-in function *trapz* is exploited to numerically evaluate the required integration. The results for both AlN and w-BN are evaluated in the following section: for both the cases, the polar layer is characterized by a thickness $d = 5\ nm$, and the density of charges in the 2DHG is considered to be $N_h = 2 \times 10^{13}\text{cm}^{-2}$, localized at $l = 0\ nm$.

4.1. AlN layer

The dispersion curve for the IF modes in *AlN* is depicted in Fig. 2, while the phonon's phase and group velocities for the optical phonons are plotted as in Fig. 5.

As noticeable, the lowest velocities happen to be in the surroundings of the resonance frequency of symmetric and antisymmetric modes. According to Eq. (21), this leads to the fulfillment of the momentum and energy conservation conditions, leading to higher emission associated to the resonance frequency. This behavior is depicted in Fig. 6, in which the number of phonons emitted with respect to the frequency is represented for three different values of hole energies E_k. The localization of the emission of phonons in a narrow range of values close to the resonant frequency is also related to the relatively high effective mass of diamond.

The scattering rates obtained via the numerical integration are depicted in Fig. 7. As predicted, the emission contributions appear for a value of hole energy equivalent to the resonance frequency of the IF modes.

Table 1
Parameters used in the calculations.

Parameter	Value
m_{lh}^*	0.303 m_0 *kg* [20]
m_{so}^*	0.394 m_0 *kg* [20]
m_{hh}^*	0.588 m_0 *kg* [20]
m^*	0.908 m_0 *kg* [20]
ρ	3515kg/m^3 [21]
ϵ_s	5.7 [21]

Table 2
AlN [13] and $w - BN$ [22] material parameters.

	AlN	w-BN
$\epsilon_{\infty}^{\perp}$	4.6	4.50
ϵ_{∞}^{y}	4.6	4.67
$\epsilon_0^{\perp}$	8.5	6.8
ϵ_0^{y}	8.5	5.1
$\omega_L^{\perp}$ (cm^{-1})	916	1281
$\omega^{\perp}$ (cm^{-1})	673	1053
ω_L^{y} (cm^{-1})	893	1258
ω^{y} (cm^{-1})	660	1006

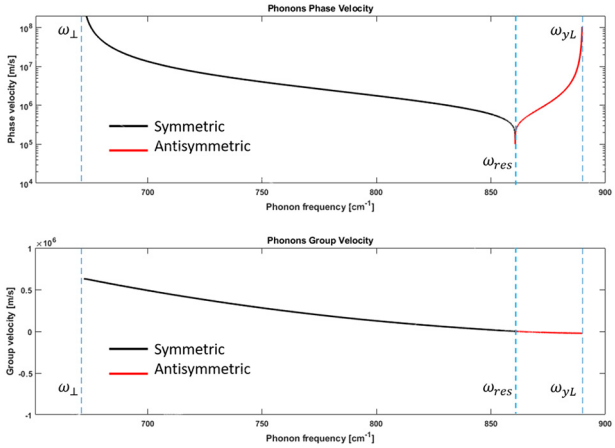

Fig. 5. Phase (top) and Group (bottom) velocity for the IF polar phonons in *AlN* layer.

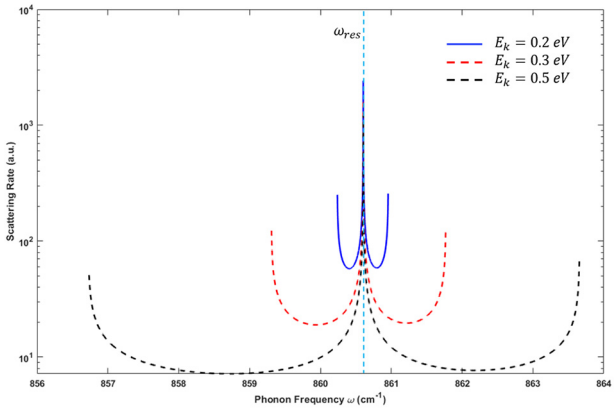

Fig. 6. Frequency distribution of the phonon emission for the case of a *AlN* layer for difference hole energies E_k.

4.2. w - BN layer

The dispersion curve for the IF modes in $w - BN$ are shown in Fig. 8. It is worth noticing that, in comparison to the curves obtained for

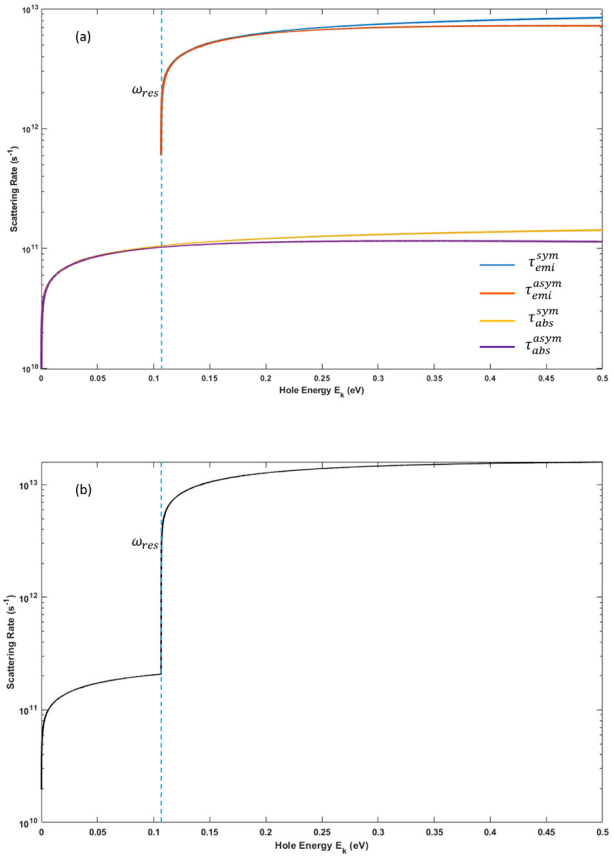

Fig. 7. Scattering rate for symmetric and antisymmetric absorption and emission (a) and their summation (b) for the *AlN* case.

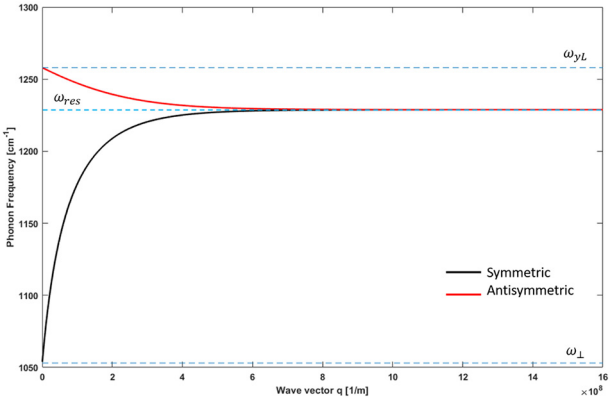

Fig. 8. Dispersion Relation for symmetric and antisymmetric IF modes in w-BN (5 nm thickness).

the case of *AlN* layer, the resonant frequency for the $w - BN$ layer happens for a higher value of phonon frequency. Based on the dispersion curve depicted in Fig. 8, the phase and group velocities for the IF optical phonons are obtained as in Fig. 9.

Also, in this case, the lowest velocities happen to be in the region surrounding the resonance frequency of symmetric and antisymmetric modes, leading to a higher emission associated to the resonance frequency, as depicted in Fig. 10. In comparison to the *AlN* case, the emission of phonons appears to be more localized in a narrow range of values close to the resonant frequency. This could be explained with the higher phonons' phase velocity in the case of $w - BN$. The scattering rates obtained via the numerical integration are plotted as in Fig. 11. The emission contribution appears for hole energies equivalent to the

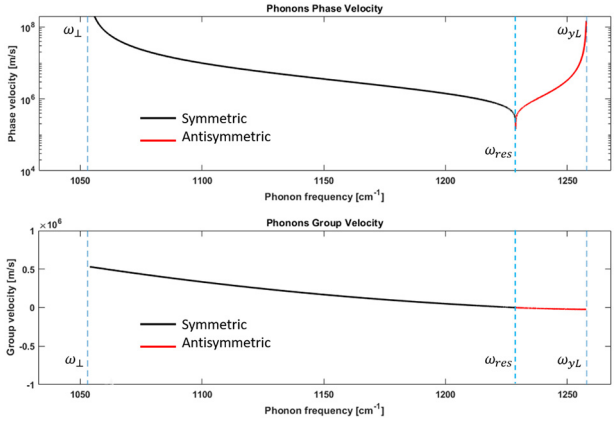

Fig. 9. Phase (top) and Group (bottom) velocity for the IF polar-phonons in w-BN layer.

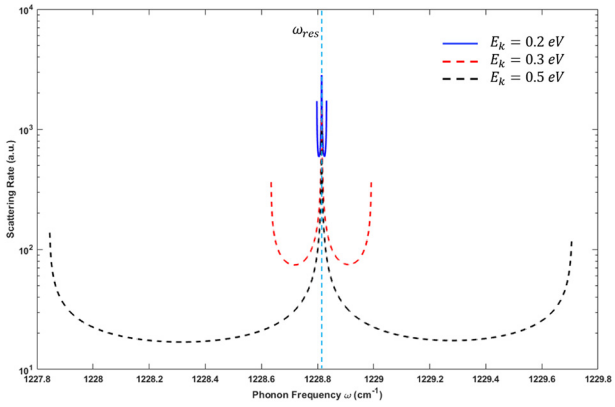

Fig. 10. Frequency distribution of the phonon emission for the case of a w-BN layer for difference hole energies E_k.

resonance frequency of the IF modes, leading to a sharp increase of the scattering rate localized at higher energies in respect to the *AlN* case.

The numerical evaluation performed for the remote IF polar phonons shows that the scattering rate is only weakly dependent on the layer thickness; this is expected physically since the Frohlich polarization, which determines the effective charge density on the surface of the layer– and therefore the interface phonon potential, is independent of the layer thickness as discussed in detail on page 68 of Ref. 13.

On the other hand, a higher density of holes localized at the diamond surface leads to an increase in the scattering rate, consistent with what has been reported in the evaluation of the same contribution for the case of *SiO$_2$/Si* [3,4]. Concerning this topic, it is important to underline that the depth of the 2DHG has been fixed to be $l = 0\ nm$. This choice is related to the representation of the 2DHG through Fang-Howard wavefunction. As depicted in Fig. 3, for such a configuration the probability to find the holes ($|\psi|^2$) is already localized a few Ångströms below the surface of diamond, in accordance with what has been discussed in the literature [24]. In order to obtain a useful comparison with the existing models trying to obtain an estimation of the 2DHG mobility in H-terminated diamond, as the one reported in [21], the mobility related to the calculated scattering rates is computed. Therefore, the conduction mass m_c^* is introduced as [21]:

$$m_c^* = \frac{(m_{lh}^{*3/2} + m_{hh}^{*3/2} + m_{so}^{*3/2})}{(m_{lh}^{*1/2} + m_{hh}^{*1/2} + m_{so}^{*1/2})} \tag{22}$$

and the 2DHG mobility is obtained as:

$$\mu = \frac{e_h \tau}{m_c^*} \tag{23}$$

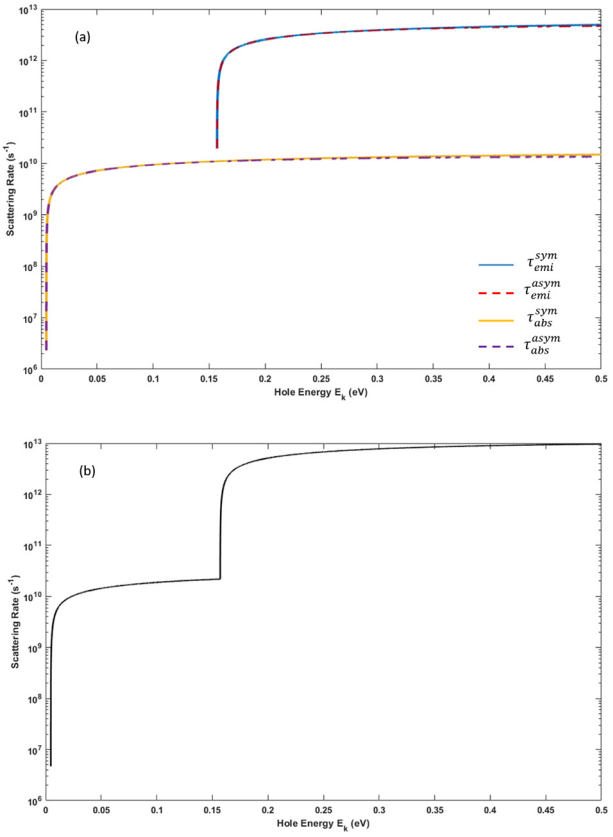

Fig. 11. Scattering rate for symmetric and antisymmetric absorption and emission (a) and their summation (b) for the w-BN case.

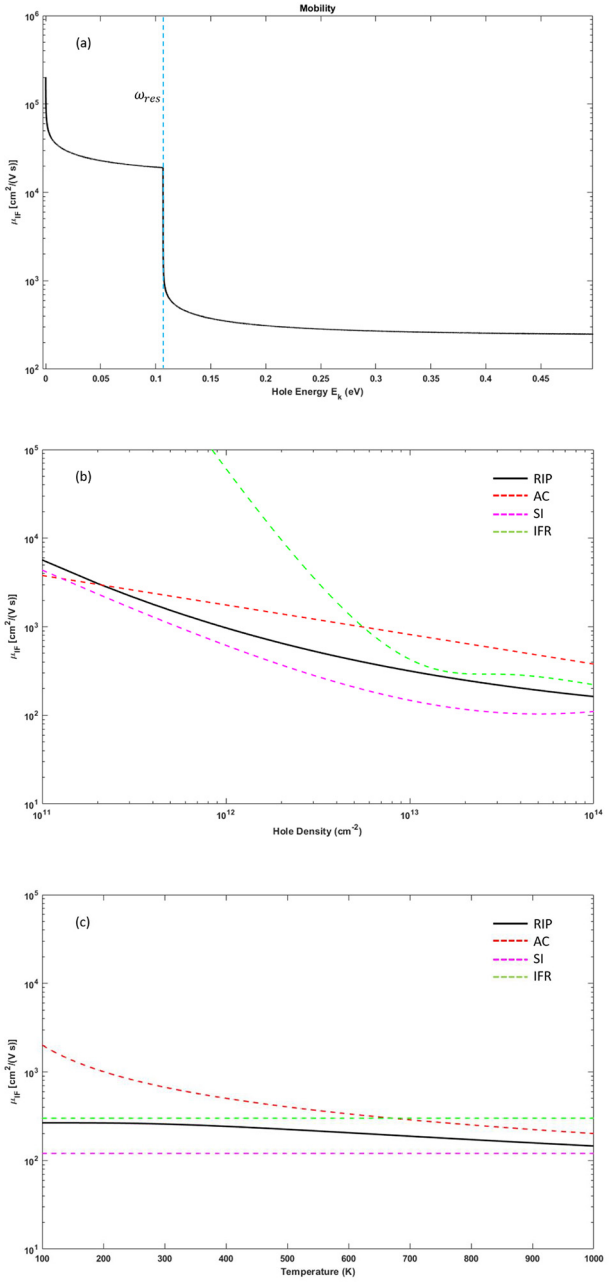

Fig. 12. 2DHG mobility considering the IF Remote polar phonons (RIP) coming from the layer of *AlN*. The dependence to hole energy (a), hole density (b) and temperature (c) is shown. Fig. 12 (b) and (c) are compared with the results of Ref. 21, which include the acoustic deformation scattering (AC), the interface roughness scattering (IFR) and the surface impurity scattering (SI).

Fig. 12 shows the mobility results for the *AlN* case. Fig. 12a shows the dependence of the mobility to the hole energy while Fig. 12b and 12c show the dependence of the mobility to the hole density and to the temperature, respectively (for $E_k = 0.5$ *e*V).

Thus, the model under investigation allows us to obtain a more faithful representation of the overall mobility in diamond-based devices realized through the insertion of polar materials.

5. Conclusions

The scattering rates of holes by remote-IF-polar phonons in the diamond structure is formulated for the first time. The results indicate clearly that the hole scattering from remote polar phonons can be comparable to, or dominate over the, other hole-phonon scattering mechanisms representing a fundamental contribution in the determination of the hole mobility. Thus, while the use of polar overlayers may contribute to desired doping effects, there is a substantial penalty associated with hole remote-polar-phonon scattering. The model adopted in the case of remote-IF-polar phonons is suitable to describe several promising polar materials, such as *AlN*, $w-BN$ and $c-BN$, MoO_3 and WO_3, currently adopted for the realization of diamond based MISFETs and HFET due to their wide-band gap. The obtained formulations facilitate taking into account the scattering mechanisms in the calculation of holes mobility in diamond, affording a more complete picture of the involved contributions.

Declaration of competing interests

The authors declare that they have no known competing financial interests or personal relationships that could have appeared to influence the work reported in this paper.

Acknowledgment

Research supported, in part, under ARL-ARO Award W911NF1920086.

Appendix A. Overlap Integral

This section demonstrates the overlap integral solution. The expression is obtained solving:

$$\langle \boldsymbol{k}' \,| e^{\mp i\boldsymbol{q}\boldsymbol{p}} e^{-qy} |\, \boldsymbol{k}\rangle = \int \Psi^* H_{def} \Psi \, dx\, dy\, dz = \frac{b^3}{2S}\int_l^L (y-l)^2 e^{-b(y-l)} e^{-qy} dy \int_{-\infty}^{+\infty} e^{\mp i\boldsymbol{q}+i(\boldsymbol{k}-\boldsymbol{k}')\boldsymbol{p}} d\boldsymbol{p}$$
$$= \frac{b^3}{2} e^{bl}\left\{ \frac{l^2 e^{-(b+q)l} - L^2 e^{-(b+q)L}}{(b+q)} + \frac{2}{(b+q)}\left[\frac{le^{-(b+q)l} - Le^{-(b+q)L}}{(b+q)} - \frac{e^{-(b+q)L} - e^{-(b+q)l}}{(b+q)^2} \right] - 2l \right.$$
$$\left. \left[\frac{le^{-(b+q)l} - Le^{-(b+q)L}}{(b+q)} - \frac{e^{-(b+q)L} - e^{-(b+q)l}}{(b+q)^2} \right] + l^2 \left[\frac{e^{-(b+q)l} - e^{-(b+q)L}}{(b+q)} \right] \right\} \delta_{\boldsymbol{k}'\parallel - \boldsymbol{k}\parallel \pm \boldsymbol{q}} = F(q)\delta_{\boldsymbol{k}'\parallel - \boldsymbol{k}\parallel \pm \boldsymbol{q}} \tag{A1}$$

where the integrals have been evaluated using:

$$\int_l^L y^2 e^{-(q+b)y} dy = \frac{l^2 e^{-(b+q)l} - L^2 e^{-(b+q)L}}{(b+q)} + \frac{2}{(b+q)}\left[\frac{le^{-(b+q)l} - Le^{-(b+q)L}}{(b+q)} - \frac{e^{-(b+q)L} - e^{-(b+q)l}}{(b+q)^2} \right] \tag{A2}$$

$$\int_l^L y\, e^{-(q+b)y}\, dy = \frac{le^{-(b+q)l} - Le^{-(b+q)L}}{(b+q)} - \frac{e^{-(b+q)L} - e^{-(b+q)l}}{(b+q)^2} \tag{A3}$$

$$\int_l^L e^{-(q+b)y}\, dy = \frac{e^{-(b+q)l} - e^{-(b+q)L}}{(b+q)} \tag{A4}$$

$$\frac{1}{S}\int_{-\infty}^{+\infty} dx \int_{-\infty}^{+\infty} dz\, e^{iz(k_z - k_z')} e^{ix(k_x - k_x')} = \delta_{\boldsymbol{k}'\parallel - \boldsymbol{k}\parallel \pm \boldsymbol{q}} \tag{A5}$$

with L representing the thickness of the diamond sample.

Appendix B. Integral Transformation

This section discusses the required calculations for the integral transformation step-by-step. First of all, the momentum conservation is enforced, in the form:

$$E_{\boldsymbol{k}\mp\boldsymbol{q}} - E_{\boldsymbol{k}} \pm \hbar\omega = \frac{\hbar^2(\boldsymbol{k}-\boldsymbol{q})^2}{2m^*} - \frac{\hbar^2\boldsymbol{k}^2}{2m^*} \pm \hbar\omega = q^2 - 2qk\cos\theta \pm \frac{2m^*\omega}{\hbar} = 0$$

$$\cos\theta = \frac{q}{2k} \pm \frac{m^*\omega}{qk\hbar}$$

$$\theta = \arccos\left(\frac{q}{2k} \pm \frac{m^*\omega}{qk\hbar} \right) \tag{B1}$$

where parabolic carrier bands are assumed. Thus, it holds:

$$\frac{d\theta}{d\omega} = \frac{-1}{\sqrt{1 - \left(\frac{q}{2k} \pm \frac{m^*\omega}{qk\hbar}\right)^2}} \left[\frac{1}{2k}\frac{\partial q}{\partial \omega} \pm \frac{m^*}{k\hbar}\left(\frac{q - \omega\frac{\partial q}{\partial \omega}}{q^2} \right) \right] = \frac{-\frac{m^*}{k\hbar}\left(\frac{\hbar}{2m^*}\frac{1}{V_g} \pm \frac{1}{q} \mp \frac{V_p}{q}\frac{1}{V_g} \right)}{\frac{m^*}{k\hbar}\sqrt{\frac{1}{m^*}\left(2E_k - \frac{E_q}{2} \mp \hbar\omega \right) - V_p^2}} = \frac{\left[\left(\pm\frac{V_p}{q} - \frac{\hbar}{2m^*} \right)\frac{1}{V_g} \mp \frac{1}{q} \right]}{\sqrt{\frac{1}{m^*}\left(2E_k - \frac{E_q}{2} \mp \hbar\omega \right) - V_p^2}} \tag{B2}$$

where $V_g = \frac{\partial\omega}{\partial q}$ and $V_p = \frac{\omega}{q}$ represent respectively phonon's group and phase velocities. It is immediate to derive,

$$\frac{dL}{dq} = \frac{\hbar^2 q}{m^*} - \frac{\hbar^2 k}{m^*}\cos\theta \pm \hbar\frac{\partial\omega}{\partial q} = \frac{\hbar^2}{m^*}\left(q - k\cos\theta \pm \frac{m^*}{\hbar}\frac{\partial\omega}{\partial q} \right) \tag{B3}$$

Recalling (B1), the derivative reported in (B3) can be expressed as:

$$\frac{dL}{dq} = \frac{\hbar^2}{m^*}\left[q - k\left(\frac{q}{2k} \pm \frac{m^*\omega}{qk\hbar} \right) \pm \frac{m^*}{\hbar}\frac{\partial\omega}{\partial q} \right] = \frac{\hbar^2}{m^*}\left(q \mp \frac{m^*\omega}{\hbar q} - \frac{q}{2} \pm \frac{m^*}{\hbar}\frac{\partial\omega}{\partial q} \right) = \frac{\hbar^2}{m^*}\left[\frac{q}{2} - \frac{m^*}{\hbar}(\pm V_p \mp V_g) \right] \tag{B4}$$

References

[1] V. Perebeinos, S.V. Rotkin, A.G. Petrov, P. Avorius, The effects of substrate phonon mode scattering on transport in carbon nanotubes, Nano Lett. 9 (1) (2009) 312–316.

[2] J.-H. Chen, J. Chaun, X. Shudong, I. Masa, M.S. Fuhrer, Intrinsic and extrinsic performance limits of graphene devices on SiO2, Nat. Nanotechnol. 3 (2008) 206–209.

[3] I. Meric, M.Y. Han, A.F. Young, B. Ozyilmaz, P. Kim, K.L. Shepard, Current saturation in zero-bandgap top-gated graphene field-effect transistors, Nat. Nanotechnol. 3 (2008) 654–659.

[4] Z.-H. Ong, M.V. Fischetti, A.Y. Serov, E. Pop, Signatures of dynamic screening in interfacial thermal transport of graphene, Phys. Rev. B 87 (19) (2013) 195404.

[5] Koh, Y. K., Lyons, A. S., Bae, M. H., Huang, B., Dorgan, V. E., Cahill, D. G., & Pop, E. (2016). Role of remote interfacial phonon (RIP) scattering in heat transport across graphene/SiO2 interfaces. Nano letters, 16, 10, 6014–6020 (2016).

[6] X. Li, E.A. Barry, J.M. Zavada, M. Buongiorno Nardelli, K.W. Kim, Surface polar phonon dominated electron transport in graphene, Appl. Phys. Lett. 97 (23) (2010) 232105.

[7] K. Hess, P. Vogl, Remote polar phonon scattering in silicon inversion layers, Solid State Commun. 30 (1979) 797.

[8] B.T. Moore, D.K. Ferry, Remote polar phonon scattering in Si inversion layers, J. Appl. Physiol. 51 (1980) 2603.

[9] J. Pernot, P.N. Volpe, F. Omn'es, P. Muret, V. Mortet, K. Haenen, T. Teraji, Hall hole mobility in boron-doped homoepitaxial diamond, Phys. Rev. B 81 (2010) 205203.

[10] P. Strobel, M. Riedel, J. Ristein, L. Ley, Surface transfer doping of diamond, Nature 430 (2004) 439.

[11] K.G. Crawford, L. Cao, D. Qi, A. Tallaire, E. Limiti, C. Verona, A.T.S. Wee, D.A.J. Moran, Enhanced surface transfer doping of diamond by V2O5 with

improved thermal stability, Appl. Phys. Lett. 108 (2016) 042103.
[12] S.A.O. Russell, L. Cao, D. Qi, A. Tallaire, K.G. Crawford, A.T.S. Wee, D.A.J. Moran, Surface transfer doping of diamond by MoO3: A combined spectroscopic and hall measurement study, Appl. Phys. Lett. 103 (2013) 202112.
[13] M.A. Stroscio, M. Dutta, Phonons in Nanostructures, Cambridge University Press, 2001.
[14] M. Imura, K. Nakajima, M. Liao, Y. Koide, H. Amano, Growth mechanism of c-axis-oriented AlN on (111) diamond substrates by metal-organic vapor phase epitaxy, J. Cryst. Growth 312 (2010) 1325.
[15] B.C. Lee, K.W. Kim, M.A. Stroscio, M. Dutta, Optical-phonon confinement and scattering in wurtzite heterostructures, Phys. Rev. B 58 (1998) 4860.
[16] J.H. Davies, The Physics of Low-dimensional Semiconductors: An Introduction, Cambridge University Press, 1997.
[17] T. Ando, A.B. Fowler, F. Stern, Electronic properties of two-dimensional systems, Rev. Mod. Phys. 54 (1982) 437.
[18] S.M. Komirenko, K.W. Kim, M. Stroscio, M. Dutta, Energy-dependent electron scattering via interaction with optical phonons in wurtzite crystals and quantum wells, Phys. Rev. B 61 (2000).
[19] K. Park, A. Mohamed, M. Dutta, M. Stroscio, C. Bayram, Electron scattering via interface optical phonons with high group velocity in Wurtzite GaN-based quantum well heterostructure, Scientific Reports 8 (2018).
[20] M. Willatzen, M. Cardona, N.E. Christensen, Linear muffin-tin-orbital and k·p calculations of effective masses and band structure of semiconducting diamond, Phys. Rev. B 50 (1994) 18054.
[21] Y. Li, J. Zhang, G.-P. Liu, Z.-Y. Ren, J.-C. Zhang, Y. Hao, mobility of two-dimensional hole gas in h-terminated diamond, Phys. Status Solidi RRL 12 (2018) 1700401.
[22] K. Karch, F. Bechstedt, Ab initio lattice dynamics of BN and AlN: covalent versus ionic forces, Phys. Rev. B 56 (1997) 7404.
[23] A. Mohamed, K. Park, C. Bayram, M. Dutta, M. Stroscio, Confined and interface optical phonon emission in GaN/InGaN double barrier quantum well heterostructures, PLoS One 14 (2019) 1.
[24] M. Imura, R. Hayakawa, H. Ohsato, E. Watanabe, D. Tsuya, T. Nagata, M. Liao, Y. Koide, J. Yamamoto, K. Ban, M. Iwaya, H. Amano, Development of AlN/diamond heterojunction field effect transistors, Diam. Relat. Mater. 24 (2012) 206.

Carbon 169 (2020) 488–500

Contents lists available at ScienceDirect

Carbon

journal homepage: www.elsevier.com/locate/carbon

Surface-acoustics phonon scattering in 2D-hole gas of diamond based FET devices

Ramji Singh [a], Giorgio Bonomo [b], Sidra Farid [a], Mahesh R. Neupane [c], A. Glen Birdwell [c], Tony G. Ivanov [c], Mitra Dutta [a, d, *], Michael A. Stroscio [a, e]

[a] Department of Electrical and Computer Engineering, University of Illinois at Chicago, Chicago, IL, 60607, USA
[b] Department of Electronics and Telecommunications, Politecnico di Torino, Torino, Piemonte, 10129, Italy
[c] CCDC U.S. Army Research Laboratory, 2800 Powder Mill Road, Adelphi, Maryland, 20783, USA
[d] Department of Physics, University of Illinois at Chicago, Chicago, IL, 60607, USA
[e] Department of Bioengineering, University of Illinois at Chicago, Chicago, IL, 60607, USA

ARTICLE INFO

Article history:
Received 11 June 2020
Received in revised form
8 July 2020
Accepted 16 July 2020
Available online 13 August 2020

Keywords:
Diamond
Phonons
Surface-acoustic phonons
Scattering rates
FETs
Heterostructures

ABSTRACT

We report on the effects of surface-acoustic phonon scattering on the charge transport behavior of diamond based FET devices. Motivated by the promising role of diamond in the realization of high power and high frequency electronic devices, the present work is focused on detailed formulation of relaxation times due to the hole-surface-acoustic phonon scattering, which appears to have been an overlooked scattering mechanism important to diamond-based devices. The matrix element, scattering rates and relaxation times have been calculated by taking into account, for the first time Rayleigh waves near the surface. This is achieved by quantizing the Rayleigh waves and using the corresponding acoustic phonon to calculate the Fermi golden rule based scattering rate of holes in the two-dimensional hole gas. The results show that the scattering of holes with surface acoustic Rayleigh waves reduced relative to scattering from bulk 3D acoustic phonons. Moreover, the mobilities are found to be higher than those based on the theory for 3D acoustic phonons. The results reveal significant insights to diamond based electronics having acoustic phonons Rayleigh waves thus opening new research endeavors.

1. Introduction

Recently, the demand for devices that can operate in harsh conditions such as high temperature, high power or high frequency has been increased significantly. Silicon, a traditional industry material is not suitable for such purposes because of its narrow band gap. As an alternative, wide band gap semiconductor materials have been explored [1]. In particular, diamond has evolved as a promising material due to its exceptional physical properties such as intrinsically high break down field (>10 MV/cm) [2], wide bandgap (5.46–5.6 eV) [3] and high thermal conductivity [4]. One of the most outstanding diamond properties includes its high carrier mobility and particularly for holes in comparison with its neighboring semiconductors such as Si or SiC [5]. Progress in the development of diamond based electronic devices has been made on a number of fronts ([IEEE TED, Vol 67, No 6, June 2020, PP-2270-2275], Crawford et al.; Pernot et al.; Zhang et al.) [6–8]. So far most of the efforts that have been directed at understanding the factors affecting conductivity are associated with external doping such as using surface acceptor oxide layers or scattering in bulk materials only [9]. Another most important factor in the mobility of diamond is the scattering mechanisms resulting from the two dimensional hole gas (2DHG) instead of bulk material which is induced at the surface of hydrogen terminated (H-terminated) diamond. There have been very few reports to date that present a detailed quantitative description of scattering mechanisms responsible for mobility limitation in 2DHG of diamond devices.

When diamond is terminated by hydrogen, it induces a negative electron affinity along with high room-temperature p-type surface conductivity [10,11]. Five scattering mechanisms that play a key role in the mobility of 2DHG in H-terminated diamond include: (1) surface impurity scattering; (2) non-polar optical phonon scattering; (3) surface roughness scattering; (4) acoustic phonon scattering and (5) interface phonon scattering [12]. In our previous

* Corresponding author. Department of Electrical and Computer Engineering, University of Illinois at Chicago, Chicago, IL, 60607, USA.
E-mail address: dutta@uic.edu (M. Dutta).

https://doi.org/10.1016/j.carbon.2020.07.078
0008-6223/

study, Bonomo et al. presented in detail the role of remote interface polar phonon modes on the electronic transport properties of diamond structures [13]. Our work laid a milestone for understanding interface phonons that penetrate to the two-dimensional hole gas (2DHG) in confined diamond structures. With the exception of Bonomo et al. work, past studies of phonon-hole interactions in diamond-based electronic devices have been modeled based by considering only bulk phonons. There is now a growing understanding of carrier-phonon interactions for confined and interface phonon modes as well as applications of phonon engineering in electronic and optoelectronic devices [14–16]. Motivated by the relatively unique properties of the 2DHG-phonon system in diamond that include high phonon velocity and close proximity of the 2DHG to the diamond interface, an examination of the difference between the bulk acoustic phonon scattering rate with holes and the interface phonon – Rayleigh wave – scattering rate with holes has been undertaken to explore the how the proper treatment of the acoustic phonons as interface phonons might affect to hole mobility. Thus, we have modeled the interaction of acoustic phonons with the 2DHG by properly taking into account the fact that the acoustic phonons in the vicinity of the 2DHG are Rayleigh waves and not bulk acoustic waves. We find substantially smaller scattering rates for the case of the Rayleigh wave interface phonons than for bulk phonons.

Considering the lattice vibrations in nanostructures, principle phenomena that alter the process of scattering include the following: firstly, reduction of hole momentum space dimensionality that originates interesting properties related to the hole-phonon interaction kinematics, secondly modifications of the phonon modes caused by the dielectric and acoustic mismatches in the nanostructure materials causes changes in properties of these materials [14]. Thus for the design of diamond based FETs, effects from surface acoustic phonon limited mobility and the screening of free carriers are of high relevance. In this work, we present a model to theoretically understand carrier transport mechanism due to surface acoustic phonon scattering in diamond based devices. The acoustic phonon scattering mechanism has been investigated using deformation-potential theory, matrix element calculations, scattering rates and taking into account the Rayleigh waves near the surface for the first time.

The paper is organized as follows: In Section II, we explain the existence of Rayleigh waves under consideration in diamond structures for surface acoustic wave analysis. Section III describe the peculiarities of the acoustic-phonon modes and its quantization. Section IV addresses the analytical expressions for the matrix elements of the hole-phonon interaction and deformation potential while Section V presents the conclusions.

2. Rayleigh surface waves existence

The surface acoustic wave relevant for this system is the Rayleigh wave. Considering the general case for Lamb waves, if the shear velocity ($V_s^{'}$) in the plate and shear velocity (V_s) in the substrate differs significantly ($Vs^{'} \gg Vs$), a generalized single Lamb wave solution exists that reduces to Rayleigh wave in the system (for which $\beta H \rightarrow 0$) where β is the wave propagation constant and H as the thickness of the elastic plate over diamond structure. For ($Vs^{'} \ll Vs$), an infinite number of solutions exists, that are divided into M_1 and M_2 series families of modes. When H (plate thickness) tends to zero, M_{11} mode tends to a Rayleigh surface wave in the substrate whereas higher M_1 and all M_2 modes appear to be leaky waves [17]. When $\beta H \rightarrow \infty$, all modes from M_{21} and above tend to be the shear velocity ($V_s^{'}$) of the plate while for $\beta H \rightarrow 0$, only the Rayleigh waves exist in the substrate (M_{11}); thus, Rayleigh waves in diamond structures are going to be analyzed solely.

3. Acoustic phonon quantization model

In this model, we have investigated scattering rates for holes in the 2-dimensional hole gas (2DHG) with surface acoustic waves for a diamond-based field effect transistor (FET). The 2DHG wave function is taken to be the Fang-Howard variational function. In this regard, the initial hole state obeys the equation as,

$$\Psi_i(r) = \langle r|k\rangle = \sqrt{\frac{b^3}{2}}\,(y-l)\,e^{-\frac{1}{2}b(y-l)}\,\frac{e^{ik_{\|}r_{\|}}}{\sqrt{S}} \tag{1}$$

While the final hole state is defined as,

$$\Psi_f(r) = \langle k^{'}|r\rangle = \sqrt{\frac{b^3}{2}}\,(y-l)\,e^{-\frac{1}{2}b(y-l)}\,\frac{e^{-ik_{\|}^{'}r_{\|}}}{\sqrt{S}} \tag{2}$$

Thus, the probability density function is given as below:

$$|\Psi_i(r)|^2 = \int_{y=l}^{\infty}\int_{z=0}^{z=Z}\int_{x=0}^{x=X} dx\,dy\,dz\left|\sqrt{\frac{b^3}{2}}(y-l)e^{-\frac{1}{2}b\,(y-l)}\frac{e^{-ik||r||}+e^{ik||r||}}{\sqrt{S}}\right| = \int_{l}^{\infty} dy\left(\sqrt{\frac{b^3}{2}}\right)^2(y-l)^2\,e^{-b(y-l)} \tag{3}$$

where $\|$ direction corresponds to x-z plane (we will drop the $\|$ subscript in the following sections), b is a variational parameter such that $b = \left(\frac{33m^*e_h^2N_h}{8\varepsilon_0\varepsilon_r\hbar^2}\right)^{\frac{1}{3}}$ [18] and $N_h = 1.8 \times 10^{17}\ m^{-2}$, [20]. S represents the area of substrate in x-z plane and l represents the depth below the surface at which the infinite barrier of triangular potential well is located which in our case is the diamond surface, hence $l = 0$ in the present case. It is to be noted that the upper limit of y has been taken to infinity because the area under the curve evaluates to 99.99% for a depth of $l + 3\,nm$, hence for all practical thickness of substrates greater than $l + 3\,nm$ it does not affect if the upper limit is taken to infinity. The probability density function is plotted in Fig. 1; it is observed that the function peaks at a depth of 660 p.m. which can be taken as the depth at which 2DHG is located.

Herein, the particle displacement expression for classical Rayleigh waves is second quantized so the matrix element of the Rayleigh wave with the hole wavefunctions corresponds to the emission or absorption of a single phonon. The Rayleigh wave amplitude has been studied extensively and the basic elements are described by Graff et al. [19] for Rayleigh waves, it is possible to formulate the displacement of the particles for a wave traveling to the right on an isotropic substrate along the z axis:

$$u_y = -A\left(\alpha_{tl}e^{-\alpha_{tl}y} - 2\frac{\alpha_{tl}\beta_R^2}{\beta_R^2+\alpha_{ts}^2}\,e^{-\alpha_{ts}y}\right)e^{i(\beta_R z-\omega t)} \tag{4}$$

$$u_z = iA\beta_R\left(e^{-\alpha_{tl}y} - 2\,\frac{\alpha_{ts}\alpha_{tl}}{\beta_R^2+\alpha_{ts}^2}\,e^{-\alpha_{ts}y}\right)e^{i(\beta_R z-\omega t)} \tag{5}$$

where β_R α_{tl} and α_{ts} represents the Rayleigh wave propagation constants respectively and the imaginary parts of the transverse wave vector components for the longitudinal and shear partial waves respectively.

For these Raleigh waves, we can write the expressions as:

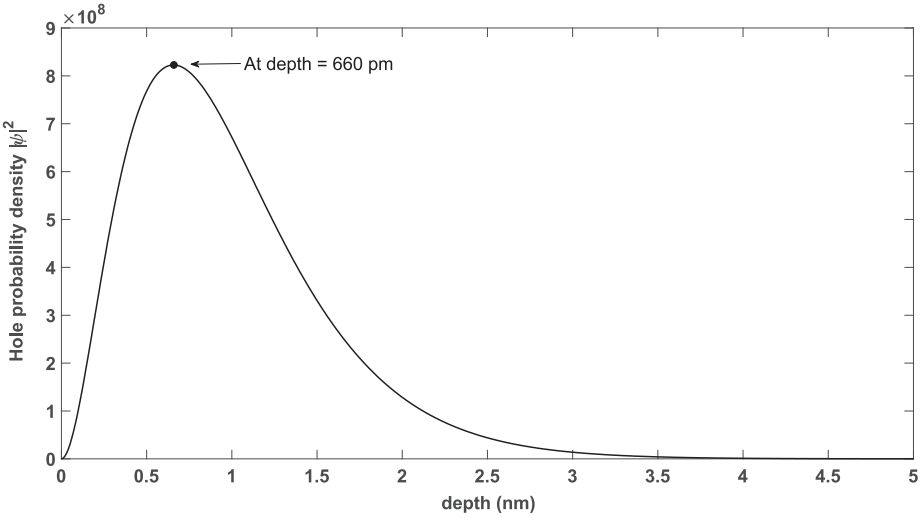

Fig. 1. Fang-Howard Probability density function for hole in 2DHG in diamond showing peak at 660 p.m.

$$\beta_R^2 - \alpha_{tl}^2 = \left(\frac{\omega}{V_l}\right)^2 \tag{6.1}$$

$$\beta_R^2 - \alpha_{ts}^2 = \left(\frac{\omega}{V_s}\right)^2 \tag{6.2}$$

$$V_R = \frac{\omega}{\beta_R} \tag{6.3}$$

Where V_R, V_l and V_s are the Rayleigh wave, longitudinal wave and shear wave velocities respectively.

The dispersion relation for these Rayleigh waves is given by;

$$4\beta_R^2\alpha_{ts}\alpha_{tl} = \left(\alpha_{ts}^2 - \beta_R^2\right)^2 \tag{7}$$

which can be approximated as presented by Auld et al. [17].

$$\frac{V_R}{V_s} = \frac{0.87 + 1.12\sigma}{1 + \sigma} \tag{8}$$

where σ is the material's Poisson ratio.

From well known standard elastic theory relations, we may recall as:

$$V_s = \sqrt{\frac{\mu}{\rho}} \tag{9.1}$$

$$V_l = \sqrt{\frac{\lambda + 2\mu}{\rho}} \tag{9.2}$$

$$\sigma = \frac{1 - 2\,(V_s/V_l)^2}{2\left[1 - 2\,(V_s/V_l)^2\right]} \tag{9.3}$$

where ρ is the density of diamond and λ and μ are the first and second Lame parameters for diamond.

Introducing the displacement vector which is known to be of the form,

$$u\,(x,y,z) = \nabla \varnothing + \nabla^*(\psi \,.\, \hat{x}) \tag{10}$$

where φ and ψ satisfy,

$$\nabla^2 \varnothing - \frac{1}{V_l^2}\frac{\partial^2 \varnothing}{\partial t^2} = 0 \tag{11.1}$$

$$\nabla^2 \psi - \frac{1}{V_s^2}\frac{\partial^2 \psi}{\partial t^2} = 0 \tag{11.2}$$

and it follows that,

$$\varnothing = Ae^{-\alpha_{tl}y}\, e^{i(\beta_R z - \omega t)} = \varnothing\,(y)\, e^{i(\beta_R z - \omega t)} \tag{11.3}$$

$$\psi = A\left(-\frac{2i\alpha_{tl}\beta_R}{\alpha_{ts}^2 + \beta_R^2}\right) e^{-\alpha_{ts}y}\, e^{i(\beta_R z - \omega t)} = \psi\,(y)\, e^{i(\beta_R z - \omega t)} \tag{11.4}$$

Thus the Rayleigh wave phonon may be quantized as outlined in Stroscio and Dutta [14] using the condition,

$$\frac{1}{cL}\int_0^c dz \int_0^{+\infty} u\,(\beta_R, y, z)\,.\,u^*\,(\beta_R, y, z)\,dy = 1 \tag{12}$$

where c and L are the normalization lengths along the horizontal and vertical axis of the diamond film respectively. Further ω_{β_R} is considered to be the angular frequency of the mode with wave vector as β_R.

The quantities,

$$\begin{aligned} u_y.\,u_y^* &= A^2\alpha_{tl}^2\left(e^{-\alpha_{tl}y} - 2\,\frac{\beta_R^2}{\beta_R^2 + \alpha_{ts}^2}e^{-\alpha_{ts}y}\right)^2 \\ &= A^2\alpha_{tl}^2\left(e^{-2\alpha_{tl}y} - 4\,\frac{\beta_R^2}{\beta_R^2 + \alpha_{ts}^2}\,e^{-(\alpha_{tl}+\alpha_{ts})y} \right. \\ &\qquad \left. + 4\frac{\beta_R^4}{\left(\beta_R^2 + \alpha_{ts}^2\right)^2}e^{-2\alpha_{ts}y}\right) \end{aligned} \tag{13}$$

and

$$u_z\,.\,u_z^* = A^2\beta_R^2\left(e^{-\alpha_{tl}y} - 2\frac{\alpha_{ts}\alpha_{tl}}{\beta_R^2 + \alpha_{ts}^2}e^{-\alpha_{ts}y}\right)^2$$

$$= A^2\beta_R^2\left(e^{-2\alpha_{tl}y} - 4\frac{\alpha_{ts}\alpha_{tl}}{\beta_R^2+\alpha_{ts}^2}e^{-(\alpha_{ts}+\alpha_{tl})y} + 4\frac{4\alpha_{ts}^2\alpha_{tl}^2}{\left(\beta_R^2+\alpha_{ts}^2\right)^2}e^{-2\alpha_{ts}y}\right) \tag{14}$$

are needed to define the integrand of the normalization condition and to obtain,

$$\frac{1}{L}\int_0^{\infty}A^2\alpha_{tl}^2\left(e^{-2\alpha_{tl}y} - 4\frac{\beta_R^2}{\beta_R^2+\alpha_{ts}^2}e^{-(\alpha_{tl}+\alpha_{ts})y} + 4\frac{\beta_R^4}{\left(\beta_R^2+\alpha_{ts}^2\right)^2}e^{-2\alpha_{ts}y}\right)dy + \frac{1}{L}\int_0^{\infty}A^2\beta_R^2\left(e^{-2\alpha_{tl}y} - 4\frac{\alpha_{ts}\alpha_{tl}}{\beta_R^2+\alpha_{ts}^2}e^{-(\alpha_{ts}+\alpha_{tl})y} + \frac{4\alpha_{ts}^2\alpha_{tl}^2}{\left(\beta_R^2+\alpha_{ts}^2\right)^2}e^{-2\alpha_{ts}y}\right)dy = 1 \tag{15}$$

Accordingly,

$$\frac{A^2\alpha_{tl}^2}{L}\left[\left.\frac{e^{-2\alpha_{tl}y}}{-2\alpha_{tl}}\right|_0^{+\infty} - 4\frac{\beta_R^2}{\beta_R^2+\alpha_{ts}^2}\left.\frac{e^{-(\alpha_{tl}+\alpha_{ts})y}}{-(\alpha_{tl}+\alpha_{ts})}\right|_0^{+\infty} + 4\frac{\beta_R^4}{\left(\beta_R^2+\alpha_{ts}^2\right)^2}\left.\frac{e^{-2\alpha_{ts}y}}{-2\alpha_{ts}}\right|_0^{+\infty}\right] +$$

$$\frac{A^2\beta_R^2}{L}\left[\left.\frac{e^{-2\alpha_{tl}y}}{-2\alpha_{tl}}\right|_0^{+\infty} - 4\frac{\alpha_{ts}\alpha_{tl}}{\beta_R^2+\alpha_{ts}^2}\left.\frac{e^{-(\alpha_{ts}+\alpha_{tl})y}}{-(\alpha_{ts}+\alpha_{tl})}\right|_0^{+\infty} + 4\frac{\alpha_{ts}^2\alpha_{tl}^2}{\left(\beta_R^2+\alpha_{ts}^2\right)^2}\left.\frac{e^{-2\alpha_{ts}y}}{-2\alpha_{ts}}\right|_0^{+\infty}\right] = 1$$

$$\frac{A^2\alpha_{tl}^2}{L}\left[\frac{1}{2\alpha_{tl}} - \frac{4\beta_R^2}{\beta_R^2+\alpha_{ts}^2}\frac{1}{\alpha_{tl}+\alpha_{ts}} + \frac{4\beta_R^4}{\left(\beta_R^2+\alpha_{ts}^2\right)^2}\frac{1}{2\alpha_{ts}}\right] + \frac{A^2\beta_R^2}{L}\left[\frac{1}{2\alpha_{tl}} - \frac{4\alpha_{ts}\alpha_{tl}}{\beta_R^2+\alpha_{ts}^2}\frac{1}{\alpha_{tl}+\alpha_{ts}} + \frac{4\alpha_{ts}^2\alpha_{tl}^2}{\left(\beta_R^2+\alpha_{ts}^2\right)^2}\frac{1}{2\alpha_{ts}}\right] = 1 \tag{16}$$

which may be simplified to,

$$A^2\left[\frac{\alpha_{tl}}{2} - \frac{4\beta_R^2\alpha_{tl}^2}{(\beta_R^2+\alpha_{ts}^2)(\alpha_{tl}+\alpha_{ts})} + \frac{2\beta_R^4\alpha_{tl}^2}{\alpha_{tl}\left(\beta_R^2+\alpha_{ts}^2\right)^2} + \frac{\beta_R^2}{2\alpha_{tl}}\right] + \left[\frac{\beta_R^2}{2\alpha_{tl}} - \frac{4\alpha_{ts}\alpha_{tl}\beta_R^2}{(\beta_R^2+\alpha_{ts}^2)(\alpha_{tl}+\alpha_{ts})} + \frac{2\beta_R^2\alpha_{ts}^2\alpha_{tl}^2}{\left(\beta_R^2+\alpha_{ts}^2\right)^2}\right] = 1 \tag{17}$$

Using the previously defined relations between the wave velocities and β_R, this last result may be simplified to,

$$A^2\left[\frac{\alpha_{tl}}{2} - \frac{(\beta_R^2+\alpha_{ts}^2)\alpha_{tl}}{\alpha_{ts}(\alpha_{tl}+\alpha_{ts})} + \frac{2\beta_R^2\alpha_{tl}}{4\alpha_{ts}^2} + \frac{\beta_R^2}{2\alpha_{tl}} - \frac{(\beta_R^2+\alpha_{ts}^2)}{(\alpha_{tl}+\alpha_{ts})} + \frac{\alpha_{tl}}{2}\right] = 1 \tag{18}$$

and it follows that,

$$A^2\left[\frac{2\alpha_{ts}^2\alpha_{tl}^2(\alpha_{tl}+\alpha_{ts})}{2\alpha_{ts}^2\alpha_{tl}(\alpha_{tl}+\alpha_{ts})} - \frac{2(\beta_R^2+\alpha_{ts}^2)\alpha_{tl}^2\alpha_{ts}}{2\alpha_{ts}^2\alpha_{tl}(\alpha_{tl}+\alpha_{ts})} + \frac{\beta_R^2\alpha_{tl}^2(\alpha_{tl}+\alpha_{ts})}{2\alpha_{ts}^2\alpha_{tl}(\alpha_{tl}+\alpha_{ts})} + \frac{\beta_R^2\alpha_{tl}^2(\alpha_{tl}+\alpha_{ts})}{2\alpha_{ts}^2\alpha_{tl}(\alpha_{tl}+\alpha_{ts})} - \frac{2\alpha_{ts}^2\alpha_{tl}\left(\beta_R^2+\alpha_{ts}^2\right)}{2\alpha_{ts}^2\alpha_{tl}(\alpha_{tl}+\alpha_{ts})}\right] = 1 \tag{19}$$

or equivalently,

$$A^2\left[\frac{2\alpha_{ts}^2\alpha_{tl}^2}{2\alpha_{ts}^2\alpha_{tl}} - \frac{2(\beta_R^2+\alpha_{ts}^2)\alpha_{tl}\alpha_{ts}}{2\alpha_{ts}^2\alpha_{tl}} + \frac{\beta_R^2\alpha_{tl}^2}{2\alpha_{ts}^2\alpha_{tl}} + \frac{\beta_R^2\alpha_{tl}^2}{2\alpha_{ts}^2\alpha_{tl}}\right] = 1 \tag{20}$$

which implies that the phonon normalization factor is,

$$A = \sqrt{\frac{2\alpha_{ts}^2\alpha_{tl}}{\beta_R^2(\alpha_{tl}-\alpha_{ts})^2 + 2\alpha_{ts}^2\alpha_{tl}(\alpha_{tl}-\alpha_{ts})}} \tag{21}$$

4. Rayleigh wave displacement pattern

Recalling the displacement expressions from eqs. (4) and (5), and noting that the displacements are real quantities, only spatial component of displacement are taken into consideration thus expressed as below;

$$u_y = Re(u_y) = -A\left(\alpha_{tl}e^{-\alpha_{tl}y} - \frac{2\alpha_{tl}\beta_R^2}{\beta_R^2+\alpha_{ts}^2}e^{-\alpha_{ts}y}\right)cos(\beta_R z) \tag{22}$$

$$u_z = Re(u_y) = A\beta_R\left(e^{-\alpha_{tl}y} - \frac{2\alpha_{tl}\alpha_{ts}}{\beta_R^2+\alpha_{ts}^2}e^{-\alpha_{ts}y}\right)sin(\beta_R z) \tag{23}$$

where S is area in x-z plane that is 1 nm^2. Now, since we know that $cos^2(\beta_R z) + sin^2(\beta_R z) = 1$, substituting for $cos(\beta_R z)$ *and* $sin(\beta_R z)$, from eqs. (1) and (2) as:

$$\frac{u_z^2}{A^2\beta_R^2\left(e^{-\alpha_{tl}y}-\frac{2\alpha_{tl}\alpha_{ts}}{\beta_R^2+\alpha_{ts}^2}e^{-\alpha_{ts}y}\right)^2}+\frac{u_y^2}{A^2\left(\alpha_{tl}e^{-\alpha_{tl}y}-\frac{2\alpha_{tl}\beta_R^2}{\beta_R^2+\alpha_{ts}^2}e^{-\alpha_{ts}y}\right)^2}=1 \tag{24}$$

The above equation represents an ellipse in y-z plane. However, for different values of y (which represents depth inside the surface) we get a family of ellipses with coordinates of center $\equiv (y,\ 0)$. The other properties of ellipse are shown below:

Major axis: along y-axis, length of major axis: $2A\left(\alpha_{tl}e^{-\alpha_{tl}y}-\frac{2\alpha_{tl}\beta_R^2}{\beta_R^2+\alpha_{ts}^2}e^{-\alpha_{ts}y}\right)$;

Coordinates of foci: $(y+c,0)$ *and* $(y-c,0)$, where expression of c is given below:

$$c=A\sqrt{\beta_R^2\left(e^{-\alpha_{tl}y}-\frac{2\alpha_{tl}\alpha_{ts}}{\beta_R^2+\alpha_{ts}^2}e^{-\alpha_{ts}y}\right)^2-\left(\alpha_{tl}e^{-\alpha_{tl}y}-\frac{2\alpha_{tl}\beta_R^2}{\beta_R^2+\alpha_{ts}^2}e^{-\alpha_{ts}y}\right)^2} \tag{25}$$

In the context of diamond we observe that u_y undergoes a phase shift by π at depth of $\frac{\lambda_R}{4}$; hence, the elliptically polarized displacement pattern undergoes change in sense of rotation from anti-clockwise to clockwise at depth of $\frac{\lambda_R}{4}$. Further, for depth less than $\frac{\lambda_R}{4}$ since the sense of rotation is anti-clockwise for direction of propagation along positive z-direction; thus, we say that such elliptical motion is retrograde in nature. Fig. 2 represents the normalized Y and Z component of Rayleigh wave displacement vectors for $\lambda_R = 500\,pm$ where as displacements patters at various depths below the surface are presented in Fig. 3.

Fig. 2 depicts the normalized Y and Z component of Rayleigh wave displacement vectors for $\lambda_R = 500$ pm. The dashed line represents the Z component and solid line represents the y-component. The y-component changes sign at y = 124.6 p.m. $\approx \frac{\lambda_R}{4}$, it is at this point the sense of rotation changes. The elliptically polarized displacement pattern becomes progressive from retrograde. The change of the sign of the y-component of displacement $\approx \frac{\lambda_R}{4}$ indicates that the ellipse representing the displacement transitions from anti-clockwise to clockwise as a function of depth. This behavior and the depth dependence of the Fang-Howard dependence on N_h – see Eq. (3) and the associated discussion – indicate that Rayleigh waves open a new avenue for tuning the mobility as a function of N_h due to the depth variation of the Rayleigh wave displacement pattern which is absent for bulk phonons.

5. Analytical expressions for hole-acoustic phonon interaction

Motivated by past phonon engineering techniques [14], the full calculation of the scattering rate of Rayleigh wave phonons with holes has been undertaken to determine the proper acoustic-phonon related mobility and compared with the previously reported result based on bulk acoustic phonons. Accordingly, in this section, the analytic expressions for the deformation potential is introduced and the scattering rates are determined by computing the matrix element obtained using Fermi-golden rule.

5.1. Deformation potential interaction

The deformation potential interaction arises from the local changes of the crystal potential that is caused by the displacement of the atoms due to an acoustic phonon. It follows that the divergence of the displacement, which is required to calculate the deformation potential, is given by:

$$\nabla.u(\boldsymbol{r}) = \nabla^2\varphi = -\frac{\omega^2}{V_l}\,\varphi = A\,e^{-\alpha_{tl}y}\,e^{i(\beta_R z-\omega t)} \tag{26}$$

Since: $q = 0\,\hat{i} + \beta_R\hat{k}$ (q is effectively a 1-D vector as Rayleigh waves only propagate along z-direction); $q.r = \beta_R z$

Hence,

$$\nabla.u(r) = = A\,e^{-\alpha_{tl}y}\,e^{iq.r}e^{i(\omega t)} = u(y)e^{iq.r}\left(dropping\ e^{i(\omega t)}\right) \tag{27}$$

Now, $U = \sqrt{\frac{\hbar}{2\rho\omega S}}\,(u(y)a_q + c.c)$

Also,

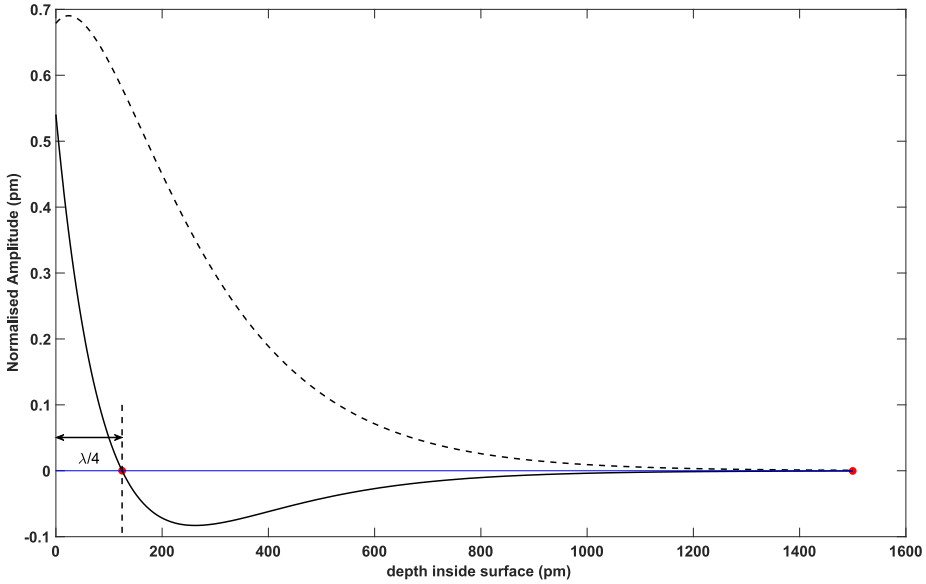

Fig. 2. Normalized Y and Z component of Rayleigh wave displacement vectors for $\lambda_R = 500$ pm. The dashed line represents the Z component and solid line represents y-component. The y-component changes sign at y = 124.6 p.m. $\approx \frac{\lambda_R}{4}$, it is at this point the sense of rotation changes. The elliptically polarized pattern becomes progressive from retrograde. (A colour version of this figure can be viewed online.)

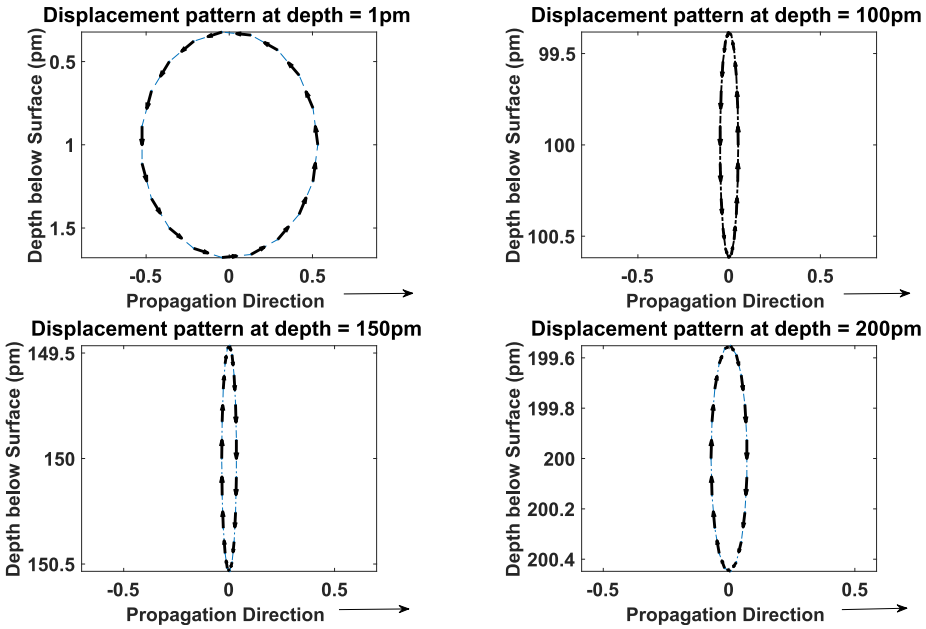

Fig. 3. Rayleigh wave displacement pattern plotted at y = 1, 100, 150 and 200 p.m. depth below surface, showing change of sense of rotation from retrograde (for depth less than $\frac{\lambda_R}{4}$) to progressive as we progress down the surface.

$$H_{def} = -E_a \sum_q \nabla.\boldsymbol{U} = -E_a \sqrt{\frac{\hbar}{2\rho\omega S}} \sum_q \nabla.(u(\boldsymbol{y}) a_q + c.c) \tag{28.1}$$

Hence,

$$H_{def} = -E_a \sum_q \frac{\omega^2}{V_l^2} \sqrt{\frac{\hbar}{2\rho\omega S}}\, u(y)\left(a_q e^{i\boldsymbol{q}.\boldsymbol{r}} + a_{-q}^{\dagger} e^{-i\boldsymbol{q}.\boldsymbol{r}}\right) \tag{28.2}$$

$$H_{def} = -C \sum_q u(y)\left(a_q e^{i\boldsymbol{q}.\boldsymbol{r}} + a_{-q}^{\dagger} e^{-i\boldsymbol{q}.\boldsymbol{r}}\right) \tag{28.3}$$

where, $C = E_a \frac{\omega^2}{V_l^2} \sqrt{\frac{\hbar}{2\rho\omega S}}$ and $u(y) = Ae^{-\alpha_{tl} y}$. The absorption of a phonon corresponds to the transition, $|N_q\rangle \rightarrow \langle N_q - 1|$ and emission of a phonon corresponds to the transition $|N_q\rangle \rightarrow \langle N_q + 1|$.

Now, the scattering rate expression is given as:

$$\frac{1}{\tau} = \frac{S}{(2\pi)^2} \int d^2q\, \frac{2\pi}{\hbar} |M^{\{a\}}(q)|^2 \delta(E_{\boldsymbol{k}'} - E_{\boldsymbol{k}} \pm \hbar\omega) \tag{29}$$

5.2. Matrix element computation

In order to evaluate the scattering rate expression we first compute matrix element $|M^{\{e,a\}}|$:

$$|M^{\{e,a\}}| = \langle k', N_q + \frac{1}{2} \pm \frac{1}{2} | H_{def} | k, N_q + \frac{1}{2} \pm \frac{1}{2} \rangle \tag{30}$$

$$|M^{\{e,a\}}| = AC \int d^3r\, \frac{e^{-k'.r + k.r \pm q.r}}{S} (y-l)^2 e^{-\alpha_{tl} y} e^{-b(y-l)} \left(N_q + \frac{1}{2} \pm \frac{1}{2}\right)$$

$$|M^{\{e,a\}}| = AC \int d^2r\, \frac{e^{-ik'.r + ik.r \pm iq.r}}{S} \int dy (y-l)^2 e^{-\alpha_{tl} y} e^{-b(y-l)} \left(N_q + \frac{1}{2} \pm \frac{1}{2}\right)$$

$$|M^{\{e,a\}}| = AC\, \delta_{\boldsymbol{k}' - \boldsymbol{k} \pm \boldsymbol{q}} F \left(N_q + \frac{1}{2} \pm \frac{1}{2}\right)$$

[Note: F is evaluated in appendix B as; $= \frac{b^3}{2} \int_l^L (y-l)^2 e^{-\alpha_{tl} y} e^{-b(y-l)}\, dy$].

Now,

$$\sum_q |M^{\{e,a\}}|^2 = A^2 C^2 F^2 \left(n_q + \frac{1}{2} \pm \frac{1}{2}\right) \frac{1}{(2\pi)^2} \int d^2q\, \delta_{\boldsymbol{k}' - \boldsymbol{k} \pm \boldsymbol{q}}$$

5.3. Scattering rate expression

Since, Scattering rate is given by Ref. [14]:

$$\frac{1}{\tau} = \frac{2\pi S}{\hbar} \sum_q |M^{\{e,a\}}|^2 \delta(E_{\boldsymbol{k}'} - E_{\boldsymbol{k}} \pm \hbar\omega) \tag{31}$$

Substituting the square of matrix element in above expression of scattering we get:

$$\frac{1}{\tau} = \frac{2\pi S}{\hbar} A^2 C^2 F^2 \frac{1}{(2\pi)^2} \int d^2q\, \delta_{\boldsymbol{k}' - \boldsymbol{k} \pm \boldsymbol{q}} \delta(E_{\boldsymbol{k}'} - E_{\boldsymbol{k}} \pm \hbar\omega) \left(N_q + \frac{1}{2} \pm \frac{1}{2}\right)$$

$$\frac{1}{\tau} = \frac{S}{2\pi\hbar} A^2 C^2 F^2 \int d^2q\, \delta_{\boldsymbol{k}' - \boldsymbol{k} \pm \boldsymbol{q}}\, \delta(E_{\boldsymbol{k}'} - E_{\boldsymbol{k}} \pm \hbar\omega) \left(N_q + \frac{1}{2} \pm \frac{1}{2}\right)$$

When above expression is simplified it becomes:

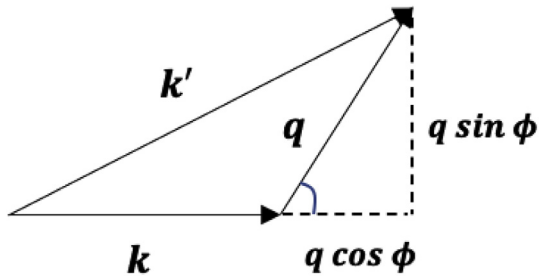

Fig. 4. Momentum conservation vector diagram for phonon absorption when.$0 \leq \varphi \leq \pi$

$$\frac{1}{\tau} = \frac{E_a^2 \omega^3 A^2}{4\pi\rho V_l^4} F^2 \int d^2q \, \delta_{\boldsymbol{k}'-\boldsymbol{k}\pm\boldsymbol{q}} \; \delta(E_{\boldsymbol{k}'} - E_{\boldsymbol{k}} \pm \hbar\omega)\left(N_q + \frac{1}{2} \pm \frac{1}{2}\right) \tag{32}$$

In the above integral the Kronecker delta function imposes the momentum conservation condition for electron-phonon interaction, whereas the Dirac delta function imposes the energy conservation. We proceed henceforth by simplifying the integrand for absorption and emission condition separately as follows:

Case a. *Condition for Absorption:* The Kronecker delta in the above integrand is expressed below through the vector equation:

$$\delta_{k'-k-q,\ 0} = \begin{cases} 1, \ if \ k' = k + q \\ 0\ , \ otherwise \end{cases}$$

We would like to point out that, the above vectors are contained in the x-z plane (azimuthal plane). Hence the incident phonon can be absorbed from any angle ranging from 0 *to* 2π spanning the entire azimuthal plane.

If $k' = k + q$, we can draw the vector diagram for incident angle in ranges $0 \leq \varphi \leq \pi$ and $\pi \leq \varphi \leq 2\pi$ respectively (we are doing this because, the argument of Dirac-delta function in eq. (32) is in terms of magnitude of vectors k'*and* k so we need to find how does the vector equation implied by Kronecker delta holds true for the condition imposed by Dirac-delta function), we draw the vector diagrams as shown in Fig. 4:

Applying Pythagoras theorem, we get:

$$\left|\boldsymbol{k}'\right|^2 = (|\boldsymbol{k}| + |\boldsymbol{q}| \cos\varphi)^2 + (|\boldsymbol{q}| \sin\varphi)^2$$

which is equivalent to, $k'^2 = k^2 + q^2 + 2kq\cos\varphi$ (33)

Similarly, if $\pi \leq \varphi \leq 2\pi$, then the vector diagram becomes as shown in Fig. 5:

Applying Pythagoras theorem, we get:

$$\left|\boldsymbol{k}'\right|^2 = (|\boldsymbol{k}| - |\boldsymbol{q}| \cos\varphi)^2 + (|\boldsymbol{q}| \sin\varphi)^2$$

which is equivalent to,

$$k'^2 = k^2 + q^2 - 2kq\cos\varphi \tag{34}$$

Case b. : Condition for Emission:

The Kronecker delta function for case of emission is given as:

$$\delta_{\boldsymbol{k}'-\boldsymbol{k}+\boldsymbol{q},\ 0} = \begin{cases} 1, \ if \ k' = k - q \\ 0\ , \ otherwise \end{cases}$$

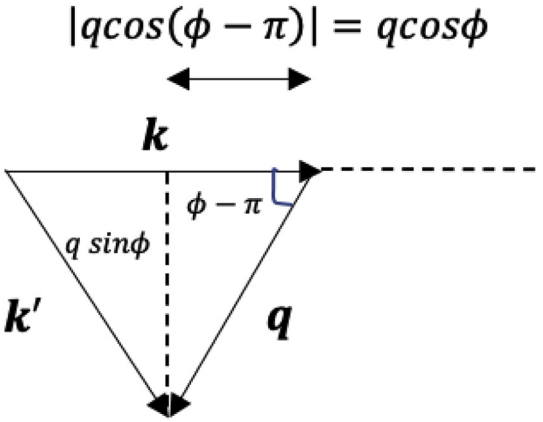

Fig. 5. Momentum conservation vector diagram for phonon absorption when.$\pi \leq \varphi \leq 2\pi$

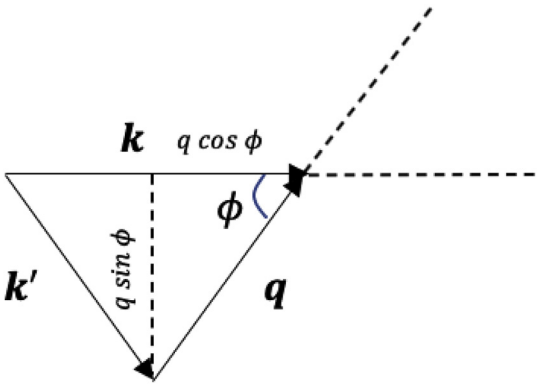

Fig. 6. Momentum conservation vector diagram for phonon emission when.$0 \leq \varphi \leq \pi$

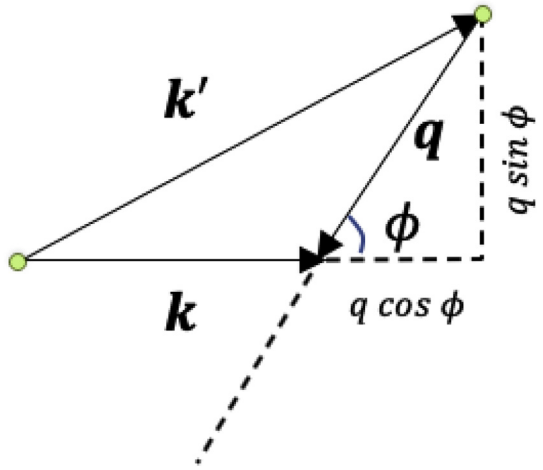

Fig. 7. Momentum conservation vector diagram for phonon emission when.$\pi \leq \varphi \leq 2\pi$

Similar to the case of absorption, the electron can emit the phonon in any angle ranging from 0 *to* 2π. We consider $0 \leq \varphi \leq \pi$ and $\pi \leq \varphi \leq 2\pi$ separately as below:

For $0 \leq \varphi \leq \pi$ the vector diagram for phonon emission is shown in Fig. 6.

$$\left|\boldsymbol{k}^{'}\right|^2 = (|\boldsymbol{k}| - |\boldsymbol{q}| \cos\varphi)^2 + (|\boldsymbol{q}| \sin\varphi)^2$$

which is equivalent to,

$$k'^2 = k^2 + q^2 - 2kq\cos\varphi \tag{35}$$

whereas for, $\pi \le \varphi \le 2\pi$: the vector diagram for phonon emission is represented in Fig. 7.

Applying Pythagoras theorem, we get:

$$\left|\boldsymbol{k}^{'}\right|^2 = (|\boldsymbol{k}| + |\boldsymbol{q}| \cos\varphi)^2 + (|\boldsymbol{q}| \sin\varphi)^2$$

which is equivalent to,

$$k'^2 = k^2 + q^2 + 2kq\cos\varphi \tag{36}$$

Now, consider the Dirac delta function for case of parabolic band:

$$\delta(E_{k'} - E_k \pm \hbar\omega_q) = \delta\left(\frac{\hbar^2 k'^2}{2m^*} - \frac{\hbar^2 k^2}{2m^*} \pm \hbar V_R q\right)$$

In the above equation we have $V_R\ q = \omega$. The upper "plus" sign corresponds to emission whereas the lower "minus" sign corresponds to absorption (we will adhere to this notation throughout this work).

Now the argument of above Dirac delta function can be simplified using eqs. (33)–(36) for emission and absorption for $0 \le \varphi \le \pi$ and $\pi \le \varphi \le 2\pi$ respectively as below:

For $0 \le \varphi \le \pi$

$$\frac{\hbar^2 k'^2}{2m^*} - \frac{\hbar^2 k^2}{2m^*} = \frac{\hbar^2}{2m^*}\left(q^2 \mp 2kq\cos\varphi\right) \tag{37}$$

And, for $\pi \le \varphi \le 2\pi$

$$\frac{\hbar^2 k'^2}{2m^*} - \frac{\hbar^2 k^2}{2m^*} = \frac{\hbar^2}{2m^*}\left(q^2 \pm 2kq\cos\varphi\right) \tag{38}$$

Thus, the argument of Dirac delta function can be written as:

$$= \delta\left(\frac{\hbar^2}{2m^*}\left(q^2 \mp 2kq\cos\varphi\right) \pm \hbar V_R q\right) \tag{39}$$

$$= \delta\left(\frac{\hbar^2 q^2}{2m^*} \mp \frac{2\hbar^2 kq\cos\varphi}{2m^*} \pm \hbar V_R q\right) \tag{40}$$

Similarly, for $\pi \le \varphi \le 2\pi$:

$$= \delta\left(\frac{\hbar^2 q^2}{2m^*} \pm \frac{2\hbar^2 kq\cos\varphi}{2m^*} \pm \hbar V_R q\right)$$

We know by the property of delta function that: $\delta(\alpha x) = \frac{1}{|\alpha|}\delta(x)$, thus applying this property above we obtain:

$$\delta(E_{k'} - E_k \pm \hbar\omega_q) = \frac{m^*}{\hbar^2 kq}\delta\left(\left(\frac{q}{2k} \pm \frac{m^* V_R}{\hbar k}\right) \mp \cos\varphi\right) \tag{41}$$

Similarly, for $\pi \le \varphi \le 2\pi$:

$$\delta(E_{k'} - E_k \pm \hbar\omega_q) = \frac{m^*}{\hbar^2 kq}\delta\left(\left(\frac{q}{2k} \pm \frac{m^* V_R}{\hbar k}\right) \pm \cos\varphi\right) \tag{42}$$

Now, defining limits of integration in Eq. (32) as below:

$$\int d^2q = \int_{q=q_{min}}^{q=q_{max}}\int_{\varphi=0}^{\varphi=2\pi} q\,dq\,d\varphi = \int_{q=q_{min}}^{q=q_{max}}\int_{\varphi=0}^{\varphi=\pi} q\,dq\,d\varphi + \int_{q=q_{min}}^{q=q_{max}}\int_{\varphi=\pi}^{\varphi=2\pi} q\,dq\,d\varphi$$

Before proceeding further we need to determine $q = q_{min}$ *and* $q = q_{max}$ in the above integral for $0 \le \varphi \le \pi$ *and* $\pi \le \varphi \le 2\pi$ for emission and absorption respectively as discussed below.

Case (i). *Emission* $(0 \le \varphi \le \pi)$: Since, $E_{\boldsymbol{k}'} - E_{\boldsymbol{k}} = -\hbar\omega$

From Eq (37): $\frac{\hbar^2 k'^2}{2m^*} - \frac{\hbar^2 k^2}{2m^*} = \frac{\hbar^2}{2m^*}(q^2 - 2kq\cos\varphi) = -\hbar V_R q$

$$\text{Where}\quad \cos\varphi = \frac{q}{2k} + \frac{m^* V_R}{\hbar k} = f(q) \tag{43}$$

The above equation puts constraints on values that q can take for a given k (hence also on hole energy). Since, $-1 \le \cos\varphi \le 1$, the limits of q is decided by intersection of $f(q)$ *and* $\cos\varphi$, as shown in graph in Fig. 8.

As we see from graph in Fig. 8, there are two sub-cases (a) $\left|\frac{m^* V_R}{\hbar k}\right| > 1$ and (b) $\left|\frac{m^* V_R}{\hbar k}\right| < 1$. We would like to point that case (a) and (b) translates to those holes for carrier energy less or greater than 0.3242 meV (because for $k = \frac{m^* V_R}{\hbar}$ the hole energy $\frac{\hbar^2 k^2}{2m^*} = \frac{m^* V_R^2}{2} = 0.3242$ meV).

For case (a), from Fig. 8 we observe that Eq. (43) has no solution

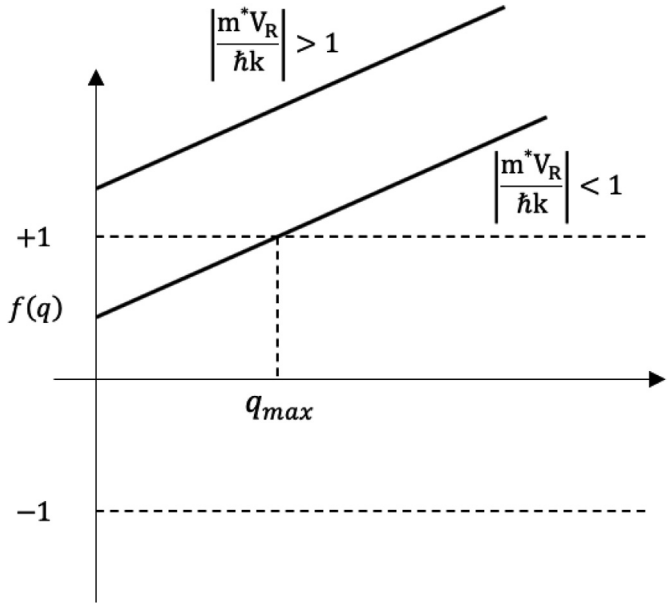

Fig. 8. Limitations on phonon wavevector for case (i) of emission from $(0 \le \varphi \le \pi)$.

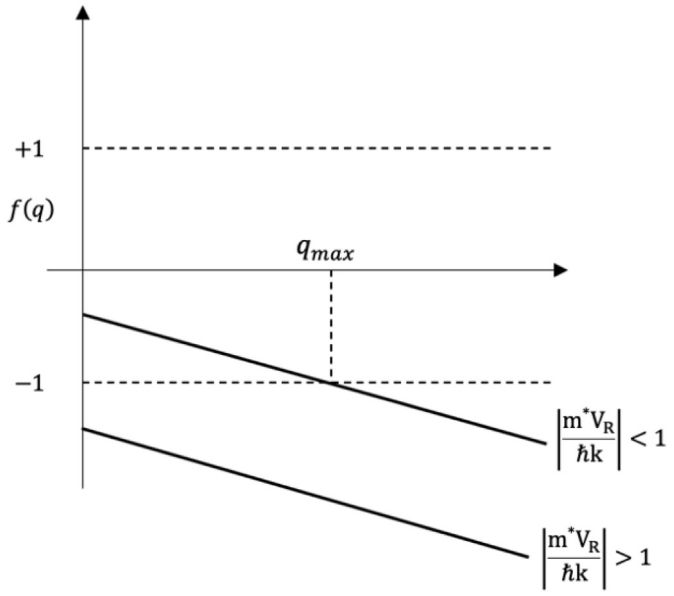

Fig. 9. Limitations on phonon wavevector for case (ii) of emission from ($\pi \leq \varphi \leq 2\pi$).

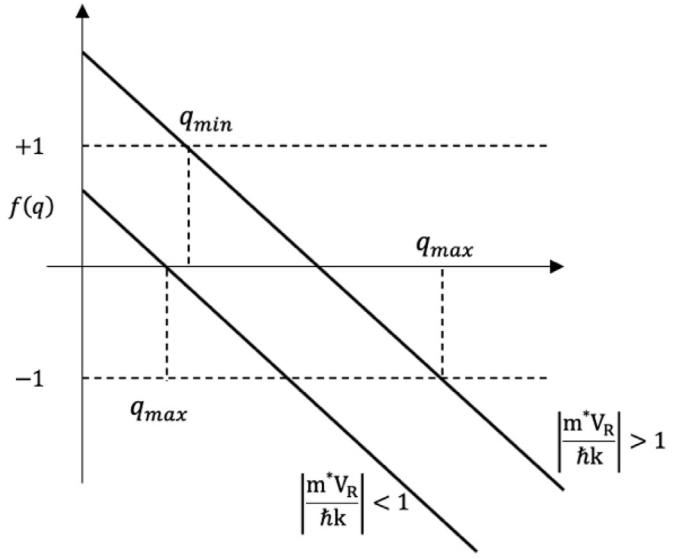

Fig. 10. Limitations on phonon wave vector for absorption – case (iii) ($0 \leq \varphi \leq \pi$).

whereas for case (b) $q_{min} = 0$;q_{max} is obtained for $f(q) = +1$ *and*we get: $q_{max} = 2k\left(1 - \frac{m^*V_R}{\hbar k}\right)$.

Case (ii). *Emission* ($\pi \leq \varphi \leq 2\pi$) as shown in Fig. 9:

$$\cos\varphi = -\frac{q}{2k} - \frac{m^*V_R}{\hbar k} = f(q) \tag{44}$$

For case (a) (hole energy < 0.3242 meV): No solution exists because no value of q satisfies equation (44). Hence, hole with energy >0.3242 meV cannot emit a phonon for emission angle. $\pi \leq \varphi \leq 2\pi$.

For case (b) (hole energy > 0.3242 meV): $q_{min} = 0$ andq_{max} is obtained for $(q) = -1$ *as* $q_{max} = 2k\left(1 - \frac{m^*V_R}{\hbar k}\right)$.

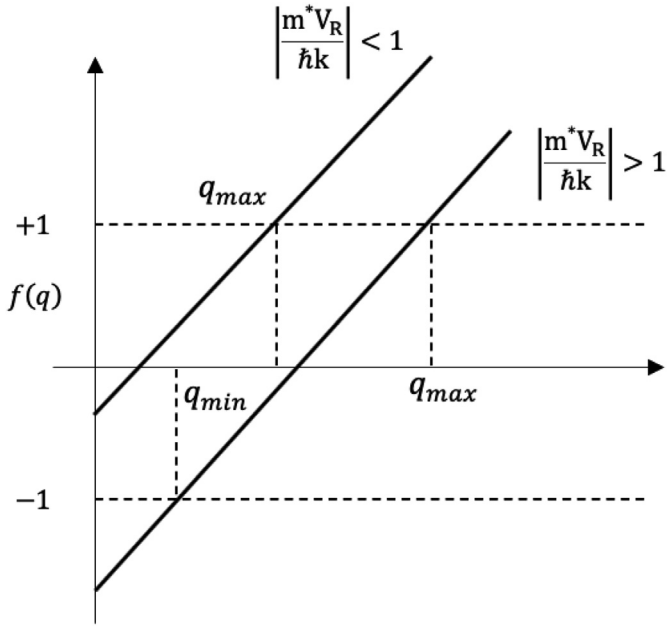

Fig. 11. Limitations on phonon wave vector for absorption – case (iv) for Absorption ($\pi \leq \varphi \leq 2\pi$).

Case (iii). *Absorption* ($0 \leq \varphi \leq \pi$) is plotted in Fig. 10 from following equation as:

$$\cos\varphi = -\frac{q}{2k} + \frac{m^*V_R}{\hbar k} = f(q) \tag{45}$$

For case (a) (hole energy < 0.3242 meV); q_{min} is obtained for $f(q) = +1$, we get $q_{min} = 2k\left(-1 + \frac{m^*V_R}{\hbar k}\right)$; q_{max} is obtained for $f(q) = -1$, we get $q_{max} = 2k\left(1 + \frac{m^*V_R}{\hbar k}\right)$.

For case (b) (hole energy > 0.3242 meV); $q_{min} = 0$ and q_{max} is obtained for $f(q) = -1$, we get: $q_{max} = 2k\left(1 + \frac{m^*V_R}{\hbar k}\right)$

Case (iv). *Absorption* ($\pi \leq \varphi \leq 2\pi$)*:* as presented in Fig. 11

$$\cos\varphi = \frac{q}{2k} - \frac{m^*V_R}{\hbar k} = f(q) \tag{46}$$

For case (a) (hole energy < 0.3242 meV) q_{min} is obtained for $f(q) = -1$, we get: $q_{min} = 2k\left(-1 + \frac{m^*V_R}{\hbar k}\right)$ and q_{max} is obtained for $f(q) = +1$, we get: $q_{max} = 2k\left(1 + \frac{m^*V_R}{\hbar k}\right)$.

For case (b) (hole energy > 0.3242 meV); $q_{min} = 0$ and q_{max} is obtained for $f(q) = +1$, we get: $q_{max} = 2k\left(1 + \frac{m^*V_R}{\hbar k}\right)$.

Hence substituting $V_R q = \omega$ *and applying* $\delta(-x) = \delta(x)$ in Eq. (32) and setting the limits for q_{min} and q_{max} as evaluated above, we write the expressions for emission and absorption as follows:

Emission:

Case (a) (hole energy < 0.3242 meV): Emission cannot occur as has been pointed out above. Hence, we observe that the condition for emission is if the hole velocity exceeds the Rayleigh wave velocity.

Case (b) (for hole energy > 0.3242 meV)

$$\frac{1}{\tau} = \frac{m^* E_a^2 V_R^3}{4\pi\hbar^2 k\rho V_l^4} \int_{q=0}^{q=2k\left(1-\frac{m^* V_R}{\hbar k}\right)} A_1 q^3\, dq \left\{ \int_{\varphi=0}^{\varphi=\pi} d\varphi\, \delta\left(\cos\varphi - \left(\frac{q}{2k}+\frac{m^* V_R}{\hbar k}\right)\right) + \int_{\varphi=\pi}^{\varphi=2\pi} d\varphi\, \delta\left(\cos\varphi + \left(\frac{q}{2k}+\frac{m^* V_R}{\hbar k}\right)\right)\right\} \tag{47}$$

$$\frac{1}{\tau} = \frac{m^* E_a^2 V_R^3}{4\pi\hbar^2 k\rho V_l^4} \int_{q=0}^{q=2k\left(1-\frac{m^* V_R}{\hbar k}\right)} A_1 q^3\, dq \left\{ 2\int_{\varphi=0}^{\varphi=\pi/2} d\varphi\, \delta\left(\cos\varphi - \left(\frac{q}{2k}+\frac{m^* V_R}{\hbar k}\right)\right) + 2\int_{\varphi=0}^{\varphi=\pi/2} d\varphi\, \delta\left(\sin\varphi - \left(\frac{q}{2k}+\frac{m^* V_R}{\hbar k}\right)\right)\right\}$$

Absorption:

Case (a) (hole energy < 0.3242 meV)

$$\frac{1}{\tau} = \frac{m^* E_a^2 V_R^3}{4\pi\hbar^2 k\rho V_l^4} \int_{q=2k\left(-1+\frac{m^* V_R}{\hbar k}\right)}^{q=2k\left(1+\frac{m^* V_R}{\hbar k}\right)} A_1 q^3\, dq \left\{ \int_{\varphi=0}^{\varphi=\pi} d\varphi\, \delta\left(\cos\varphi + \left(\frac{q}{2k}-\frac{m^* V_R}{\hbar k}\right)\right) + \int_{\varphi=\pi}^{\varphi=2\pi} d\varphi\, \delta\left(\cos\varphi - \left(\frac{q}{2k}-\frac{m^* V_R}{\hbar k}\right)\right)\right\}$$

$$\frac{1}{\tau} = \frac{m^* E_a^2 V_R^3}{4\pi\hbar^2 k\rho V_l^4} \int_{q=2k\left(-1+\frac{m^* V_R}{\hbar k}\right)}^{q=2k\left(1+\frac{m^* V_R}{\hbar k}\right)} A_1 q^3 dq \left\{ 2\int_{\varphi=0}^{\varphi=\pi/2} d\varphi\, \delta\left(\cos\varphi - \left(\frac{q}{2k}-\frac{m^* V_R}{\hbar k}\right)\right) + 2\int_{\varphi=0}^{\varphi=\pi/2} d\varphi\, \delta\left(\sin\varphi - \left(\frac{q}{2k}-\frac{m^* V_R}{\hbar k}\right)\right)\right\} \tag{48}$$

Case (b) (hole energy > 0.3242 meV)

$$\frac{1}{\tau} = \frac{m^* E_a^2 V_R^3}{4\pi\hbar^2 k\rho V_l^4} \int_{q=0}^{q=2k\left(1+\frac{m^* V_R}{\hbar k}\right)} A_1 q^3 dq \left\{ \int_{\varphi=0}^{\varphi=\pi} d\varphi\, \delta\left(\cos\varphi + \left(\frac{q}{2k}-\frac{m^* V_R}{\hbar k}\right)\right) + \int_{\varphi=\pi}^{\varphi=2\pi} d\varphi\, \delta\left(\cos\varphi - \left(\frac{q}{2k}-\frac{m^* V_R}{\hbar k}\right)\right)\right\}$$

$$\frac{1}{\tau} = \frac{m^* E_a^2 V_R^3}{4\pi\hbar^2 k\rho V_l^4} \int_{q=0}^{q=2k\left(1+\frac{m^* V_R}{\hbar k}\right)} A_1 q^3 dq \left\{ 2\int_{\varphi=0}^{\varphi=\pi/2} d\varphi\, \delta\left(\cos\varphi - \left(\frac{q}{2k}-\frac{m^* V_R}{\hbar k}\right)\right) + 2\int_{\varphi=0}^{\varphi=\pi/2} d\varphi\, \delta\left(\sin\varphi - \left(\frac{q}{2k}-\frac{m^* V_R}{\hbar k}\right)\right)\right\} \tag{49}$$

To simplify the Dirac-delta function, we recall Eq. (8.14) from Stroscio & Dutta [14] as follows:

$$\int g(\varphi)\, \delta(f(\varphi) - a)\, d\varphi = \left.\frac{g(\varphi)}{|df/d\varphi|}\right|_{\varphi=\varphi_0}$$

where. $f(\varphi_0) = a$

Evaluating the first integral,

$$\int_{\varphi=0}^{\varphi=\pi/2} d\varphi\, \delta\left(\cos\varphi - \left(\frac{q}{2k} \pm \frac{m^* V_R}{\hbar k}\right)\right)$$

On comparing the integral in Eqs. (47) and (48) with Eq. (8.14) we observe:

$$g(\varphi) = 1$$

$$f(\varphi) = \cos\varphi$$

$$a = f(\varphi_0) = \cos\varphi_0 = \left(\frac{q}{2k} \pm \frac{m^* V_R}{\hbar k}\right)$$

Hence,

$$\frac{df}{d\varphi} = -\sin\varphi$$

$$\left|\frac{df}{d\varphi}\right|_{\varphi=\varphi_0} = |\sin\varphi_0| = \sqrt{|1-\cos^2\varphi_0|}$$

Hence,

$$\left|\frac{df}{d\varphi}\right|_{\varphi=\varphi_0} = \sqrt{\left|1-\left(\frac{q}{2k} \pm \frac{m^* V_R}{\hbar k}\right)^2\right|}$$

$$\left.\frac{g(\varphi)}{|df/d\varphi|}\right|_{\varphi=\varphi_0} = \frac{1}{\sqrt{\left|1-\left(\frac{q}{2k} \pm \frac{m^* V_R}{\hbar k}\right)^2\right|}}$$

Similarly,

$$\int_{\varphi=0}^{\varphi=\pi/2} d\varphi\, \delta\left(\sin\varphi - \left(\frac{q}{2k}-\frac{m^* V_R}{\hbar k}\right)\right) = \frac{1}{\sqrt{\left|1-\left(\frac{q}{2k} \pm \frac{m^* V_R}{\hbar k}\right)^2\right|}}$$

Hence substituting in the above results for Dirac-delta function and as well as for $A_1 = A^2F^2\left(N_q + \frac{1}{2}\pm\frac{1}{2}\right) = \frac{A_2}{q}\frac{b^6}{(nq+b)^6} e^{-2nql}\left(N_q + \frac{1}{2}\pm\frac{1}{2}\right)$ (see appendix B for simplification) we obtain following expressions as plotted in Fig. 12:

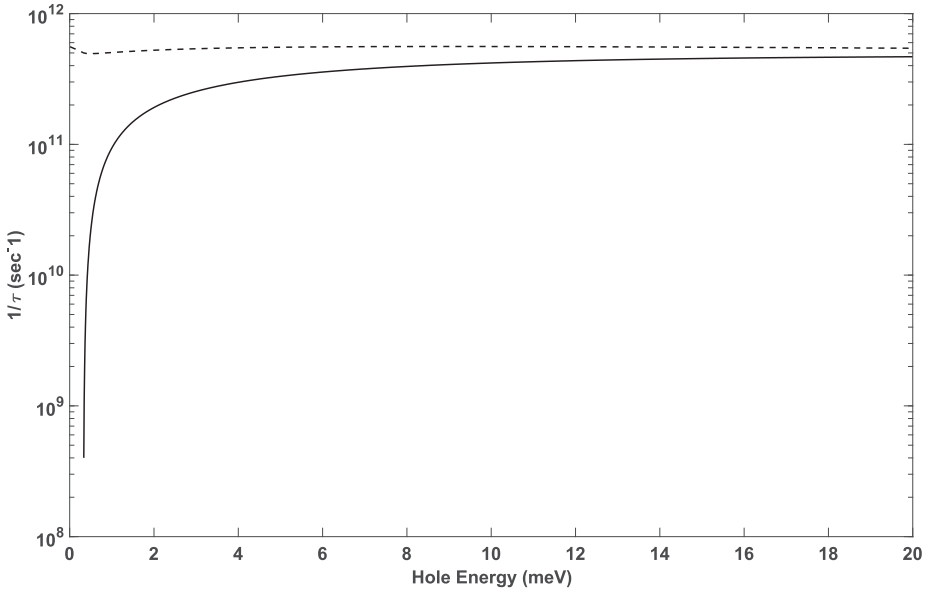

Fig. 12. Emission and absorption scattering rates for 2DHG at 300 K - solid line represents emission and dashed line represents absorption - for 2DHG depth of 660 p.m.

Emission (for hole energy > 0.3242 meV):

$$\frac{1}{\tau} = \frac{m^* E_a^2 V_R^3 A_2}{\pi\hbar^2 k\rho V_l^4} \int_{q=0}^{q=2k\left(1-\frac{m^* V_R}{\hbar k}\right)} dq \frac{b^6 e^{-2\alpha_{tl} l}}{(\alpha_{tl}+b)^6} \frac{q^2}{\sqrt{\left|1-\left(\frac{q}{2k}+\frac{m^* V_R}{\hbar k}\right)^2\right|}} (N_q+1) \tag{50}$$

Absorption (for hole energy < 0.3242 meV):

$$\frac{1}{\tau} = \frac{m^* E_a^2 V_R^3 A_2}{\pi\hbar^2 k\rho V_l^4} \int_{q=2k\left(-1+\frac{m^* V_R}{\hbar k}\right)}^{q=2k\left(1+\frac{m^* V_R}{\hbar k}\right)} dq \frac{b^6 e^{-2\alpha_{tl} l}}{(\alpha_{tl}+b)^6} \frac{q^2}{\sqrt{\left|1-\left(\frac{q}{2k}-\frac{m^* V_R}{\hbar k}\right)^2\right|}} (N_q) \tag{51}$$

Absorption (for hole energy > 0.3242 meV):

$$\frac{1}{\tau} = \frac{m^* E_a^2 V_R^3 A_2}{\pi\hbar^2 k\rho V_l^4} \int_{q=0}^{q=2k\left(1+\frac{m^* V_R}{\hbar k}\right)} dq \frac{b^6 e^{-2\alpha_{tl} l}}{(\alpha_{tl}+b)^6} \frac{q^2}{\sqrt{\left|1-\left(\frac{q}{2k}-\frac{m^* V_R}{\hbar k}\right)^2\right|}} (N_q) \tag{52}$$

These rates are nearly an order of magnitude smaller than the rates based on equipartition formula reported by Ridley et al. [21], for the case of a 3D system. Our results are based on 2DHG scattering events when the acoustic phonons are those of the surface acoustic Rayleigh waves as opposed to earlier results that assume the acoustic phonons are bulk 3D acoustic phonons. The 2D mobilities calculated based on these Rayleigh waves using the following expression for the mobility of this 2D system is calculated as:

$$\mu = \frac{e}{m}\frac{<E_k\tau_m>}{<E_k>} = \frac{\int_0^\infty E_k\, exp(-E_k/k_BT)\,\tau_m dE_k}{\int_0^\infty E_k\, exp(-E_k/k_BT)\,dE_k} = 2131.5\ cm^2 \Big/ V.s$$

when T = 300 K. The mean free path of hole is given by:

$$\tau_m(E_k) = \frac{1}{\left(\frac{1}{\tau_e(E_k)}+\frac{1}{\tau_a(E_k)}\right)}$$

Fig. 13 depicts the hole mobility due to hole—Rayleigh-wave scattering as a function of temperature with a comparison with corresponding mobility for bulk acoustic phonons as reported by Li et al. [12]. In calculating this mobility, the depth of the 2DHG ($y \approx 2/b$) has been evaluated for the corresponding hole density as reported in Ref. 20 for the above temperature range has been used in these calculations. Fig. 13. The mobility for the case of hole scattering from Rayleigh waves is seen to be approximately a factor of three larger than that based on hole scattering from bulk acoustic phonons. As discussed, Li et al. [12], the mobilities due to interface roughness scattering and surface impurity scattering are lower than the mobility for acoustic phonon scattering for currently realizable roughness and impurity parameters. Thus the current experimental mobilities are much lower than our calculations since these effects currently dominate the results. Of course, for low level impurities and for lower levels of surface roughness, the dominant mobility-determining effect will be due to hole-acoustic phonon scattering and, as usual, carrier-phonon scattering sets the fundamental limit on mobility.

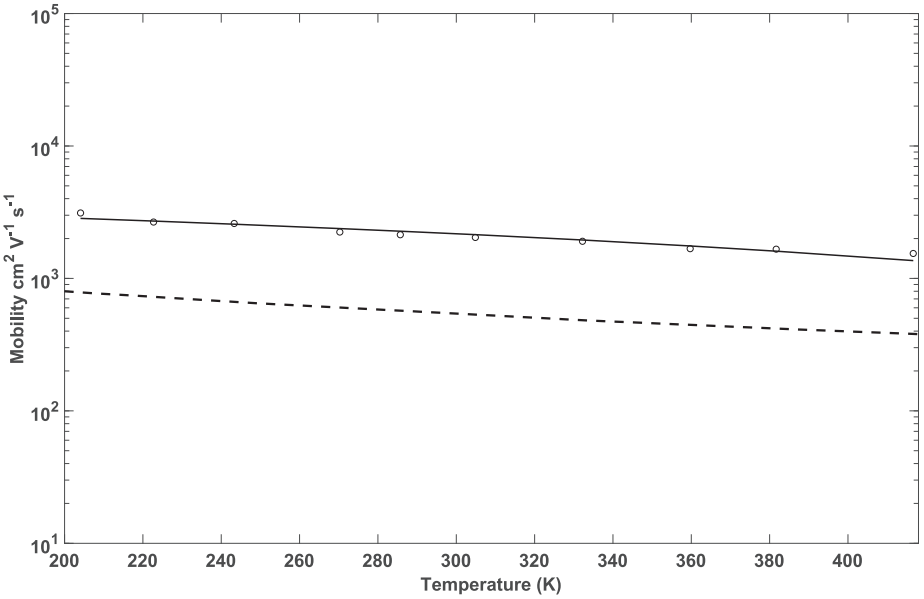

Fig. 13. Hole mobility due to hole—Rayleigh-wave scattering of this work (shown in solid line) compared with the mobility for hole-bulk acoustic phonon scattering (shown in dashed line) as reported in Ref. [13]. In our work the hole density dependence on temperature has been taken as reported in Refs. [20] for the above temperature range.

6. Conclusions

Herein, we have calculated the scattering rates for holes in the 2DHG that scatter from surface acoustic waves – Rayleigh waves – as opposed to bulk 3D acoustic phonons of previous treatments for hole scattering in diamond based FETs. It is found that the scattering rates for Rayleigh wave phonons are about an order smaller than the rates based on 3D acoustic phonons. Moreover, the mobilities are found to be higher than those based on the theory for 3D acoustic phonons summarized by Ridley et al. [21]. These higher mobilities associated with the intrinsic acoustic phonon scattering process for Rayleigh waves as opposed to bulk acoustic phonons represent an unanticipated benefit of diamond-based devices with the 2DHG in the region where the acoustic phonons are Rayleigh waves instead of bulk acoustic phonons.

CRediT authorship contribution statement

Ramji Singh: Formal analysis, Investigation. **Giorgio Bonomo:** Formal analysis, Investigation. **Sidra Farid:** Investigation, Writing - review & editing. **Mahesh R. Neupane:** Resources, Writing - review & editing. **A. Glen Birdwell:** Resources, Writing - review & editing. **Tony G. Ivanov:** Funding acquisition, Writing - review & editing. **Mitra Dutta:** Conceptualization, Validation, Investigation, Supervision. **Michael A. Stroscio:** Conceptualization, Methodology, Investigation, Supervision.

Declaration of competing interest

The authors declare that they have no known competing financial interests or personal relationships that could have appeared to influence the work reported in this paper.

Acknowledgment

The authors gratefully acknowledge useful conversations with Dr. Bo Hsu. The authors also would like to acknowledge Diamond Electronic Team at CCDC-ARL for providing device related insights during the course of this research. Research supported, in part, under ARL-ARO Award W911NF1920086.

Appendix A

$$F = \frac{b^3}{2}\int_l^L (y-l)^2\, e^{-\alpha_{tl}y}\, e^{-b(y-l)}\, dy$$

$$F = \frac{b^3}{2} e^{-\alpha_{tl}l}\int_l^L (y-l)^2\, e^{-(\alpha_{tl}+b)(y-l)}\, dy$$

Let, $\alpha_{tl} + b = m$ and $y - l = x$ and let $l_0 = L - l$

$$F = \frac{b^3}{2} e^{-\alpha_{tl}l}\int_0^{l_0} (x)^2\, e^{-mx}\, dy$$

$$F = \frac{b^3}{2}\left[-\frac{l_0^2\, e^{-ml_0}}{m} - \frac{2l_0\, e^{-ml_0}}{m^2} - \frac{2\left(e^{-ml_0}-1\right)}{m^3}\right]$$

Substituting for m and l_0 , we get:

$$F = \frac{b^3}{2}\left[-\frac{(L-l)^2\, e^{-\alpha_{tl}L}\, e^{-bl_0}}{(\alpha_{tl}+b)} - \frac{2(L-l)\, e^{-\alpha_{tl}L}\, e^{-bl_0}}{(\alpha_{tl}+b)^2} - \frac{2\, e^{-\alpha_{tl}l}\left(e^{-\alpha_{tl}L}\, e^{-bl_0}-1\right)}{(\alpha_{tl}+b)^3}\right]$$

Hence, Now squaring the above expression we get:

$$F^2 = \frac{b^6}{4}\left[\frac{(L-l)^4\, e^{-2\alpha_{tl}L}\, e^{-2b(L-l)}}{(\alpha_{tl}+b)^2} + \frac{4(L-l)^2\, e^{-2\alpha_{tl}L}\, e^{-b(L-l)}}{(\alpha_{tl}+b)^4}\right.$$
$$\left(e^{-bl_0} + \left(e^{-\alpha_{tl}L}\, e^{-b(L-l)} - 1\right)\right) + \frac{8(L-l)\, e^{-2\alpha_{tl}L}\, e^{-b(L-l)}}{(\alpha_{tl}+b)^5}$$
$$\left(e^{-\alpha_{tl}L}\, e^{-b(L-l)} - 1\right) + \frac{4(L-l)^3\, e^{-2\alpha_{tl}L}\, e^{-2b(L-l)}}{(\alpha_{tl}+b)^3}$$
$$\left. + \frac{4e^{-2\alpha_{tl}l}}{(\alpha_{tl}+b)^6}\left(e^{-\alpha_{tl}L}\, e^{-b(L-l)} - 1\right)^2\right]$$

Also,

$$\lim_{L\to\infty}(F)^2 = \frac{b^6}{4}\left(\frac{4e^{-2\alpha_{tl}l}}{(\alpha_{tl}+b)^6}\right) = \frac{b^6 e^{-2\alpha_{tl}l}}{(\alpha_{tl}+b)^6}$$

Appendix B

$$A^2 = \frac{2\alpha_{ts}^2\alpha_{tl}/(\alpha_{tl}-\alpha_{ts})^2}{\beta_R^2 + \alpha_{ts}^2\alpha_{tl}/(\alpha_{tl}-\alpha_{ts})}$$

Since, $\beta_R = q$

$$A^2 = \frac{2\alpha_{ts}^2\alpha_{tl}/(\alpha_{tl}-\alpha_{ts})^2}{q^2 + \alpha_{ts}^2\alpha_{tl}/(\alpha_{tl}-\alpha_{ts})}$$

Moreover, α_{tl} and α_{ts} are not constants they are dependent on $\beta_R$as follows :

$$\alpha_{ts}^2 = \beta_R^2 - \left(\frac{\omega}{V_s}\right)^2$$

And,

$$\alpha_{tl}^2 = \beta_R^2 - \left(\frac{\omega}{V_l}\right)^2$$

But, we already know the relation between V_R and V_s as follows:

Hence, to simplify the expressions of F and A we can express α_{tl} and α_{ts} as below:

$$\alpha_{ts}^2 = \beta_R^2 - \left(\frac{\omega}{V_s}\right)^2$$

$$\alpha_{ts}^2 = \left(1 - \left(\frac{V_R}{V_s}\right)^2\right)\beta_R^2$$

$$\alpha_{ts} = \beta_R\sqrt{\left(1 - \left(\frac{V_R}{V_s}\right)^2\right)}$$

So, let

$$\alpha_{ts} = s\beta_R = sq$$

And,

$$\alpha_{tl} = n\beta_R = nq$$

Where, $s = \sqrt{\left(1 - \left(\frac{V_R}{V_s}\right)^2\right)}$ *and* $n = \sqrt{\left(1 - \left(\frac{V_R}{V_l}\right)^2\right)}$

Now, A can be simplified as follows:

$$A^2 = \frac{2\alpha_{ts}^2\alpha_{tl}/(\alpha_{tl}-\alpha_{ts})^2}{q^2 + \alpha_{ts}^2\alpha_{tl}/(\alpha_{tl}-\alpha_{ts})}$$

$$A^2 = \frac{2s^2n/(n-s)^2}{q(1+s^2n/(n-s))} = \frac{A_2}{q}$$

References

[1] K. Tsukioka, Scattering mechanisms of carriers in natural diamond, Jpn. J. Appl. Phys. 40 (5R) (2001) 3108.
[2] E.A. Konorova, Y.A. Kuznetsov, V.F. Sergienko, S.D. Tkachenko, A.V. Tsikunov, A.V. Spitsyn, Y.Z. Danyushevskii, Impact ionization in semiconductor structures made of ion-implanted diamond, Sov. Phys. Semiconduct. 17 (1983) 146–149.
[3] C.D. Clark, P.J. Dean, P.V. Harris, Proc. Roy. Soc. (London) A277 (1964) 312–329.
[4] R. Berman, P.R.W. Hudson, M. Martinez, J. Phys. Chem. 8 (21) (1975) L430–L434.
[5] F. Nava, C. Canali, C. Jacoboni, L. Reggiani, S. Kozlov, Electron effective masses and lattice scattering in natural diamond, Solid State Commun. 33 (4) (1980) 475–477.
[6] K.G. Crawford, L. Cao, D. Qi, A. Tallaire, E. Limiti, C. Verona, A.T. Wee, D.A. Moran, Enhanced surface transfer doping of diamond by V2O5 with improved thermal stability, Appl. Phys. Lett. 108 (4) (2016), 042103.
[7] J. Pernot, P.N. Volpe, F. Omnes, P. Muret, Hall hole mobility in boron-doped homoepitaxial diamond, Phys. Rev. B 81 (2010), 205203.
[8] J.F. Zhang, W.J. Chen, Z.Y. Ren, K. Su, P.Z. Yang, Z.Z. Hu, J.C. Zhang, Y. Hao, Characterization and mobility analysis of normally off hydrogen-terminated diamond metal–oxide–semiconductor field-effect transistors, Phys. Status Solidi 217 (1) (2020) 1900462.
[9] J. Ristein, F. Maier, M. Riedel, M. Stammer, L. Ley, Diamond surface conductivity experiments and photoelectron spectroscopy, Diam. Relat. Mater. 10 (3–7) (2001) 416–422.
[10] M.I. Landstrass, K.V. Ravi, Resistivity of chemical vapor deposited diamond films, Appl. Phys. Lett. 55 (1989) 975–977.
[11] F. Maier, M. Riedel, B. Mantel, J. Ristein, L. Ley, Origin of surface conductivity in diamond, Phys. Rev. Lett. 85 (Nov 2000) 3472–3475.
[12] Y. Li, J.F. Zhang, G.P. Liu, Z.Y. Ren, J.C. Zhang, Y. Hao, Mobility of two-dimensional hole gas in H-terminated diamond, Phys. Status Solidi Rapid Res. Lett. 12 (3) (2018) 1700401.
[13] G. Bonomo, A. Mohamed, S. Farid, K. Park, M. Dutta, M.A. Stroscio, Contribution of remote interface polar phonons in the hole mobility of diamond, Diam. Relat. Mater. 101 (2020) 107650.
[14] Michael A. Stroscio, Dutta Mitra, Phonons in Nanostructures, Cambridge University Press, 2001.
[15] K. Park, M.A. Stroscio, C. Bayram, Investigation of electron mobility and saturation velocity limits in gallium nitride using uniaxial dielectric continuum model, J. Appl. Phys. 121 (24) (2017), 245109-1-8.
[16] S.M. Komirenko, K.W. Kim, M.A. Stroscio, M. Dutta, Energy dependent electron scattering via interactions with optical phonons in wurtzite crystals and quantum wells, Phys. Rev. B 61 (2000) 2034.
[17] B.A. Auld, Acoustic Fields and Waves in Solids, vol. 2, John Wiley & Sons, New York, 1973.
[18] J.H. Davies, The Physics of Low-Dimensional Semiconductors: an Introduction, Cambridge University Press, 1997.
[19] K.F. Graff, Wave Motion in Elastic Solids, Courier Corporation, 1991.
[20] Hiroshi Kawarada, Hydrogen-terminated diamond surfaces and interfaces, Surf. Sci. Rep. 26 (7) (1996) 205–208.
[21] B.K. Ridley, Quantum Processes in Semiconductors, Oxford University Press, Oxford, 1988, p. 99.

Phonon-Dominated Mobilities for Carriers in a Diamond Field Effect Transistor With a cBN Overlayer

Ramji Singh, Michael A. Stroscio, *Life Fellow, IEEE*, and Mitra Dutta, *Life Fellow, IEEE*

***Abstract*— In this letter we investigate phonon-dominated mobilities for carriers in a diamond field effect transistor with a cubic Boron Nitride (cBN) overlayer. We investigate the intra-subband scattering due to interaction of electrons with acoustic phonons, treated properly as quantized surface acoustic Rayleigh waves, and include, for the first time, the interaction with remote polar phonons originating in the cBN overlayer. We conclude that the surface acoustic phonon scattering is the dominant mechanism limiting the mobility of electrons for temperatures below 375 K.**

***Index Terms*— cBN, diamond, remote polar phonon, surface acoustic phonon, Rayleigh wave, scattering, FET.**

I. Introduction

DIAMOND based field effect transistors (FETs) have attracted widespread attention due to the possibility of achieving high carrier mobilities of approximately 2500 cm^2/V-sec for the holes in the two-dimensional hole gas formed near the surface of a diamond FET [1]. Recent studies of diamond-cBN structures [2], [3] have suggested the possibility of producing a two-dimensional electron gas (2DEG) in nearly lattice matched diamond-cBN heterostructures. Stimulated by the possibility of fabricating n-type FETs, we have modeled the dominant mobility-limiting carrier-phonon scattering for electrons in the 2DEG formed in the diamond near the diamond-cBN heterojunction; in determining the dominant carrier-phonon limiting mobilities, it is essential to not only model the commonly considered scattering of carriers by acoustic phonons but also carrier scattering by remote polar phonons that originate from the polar cBN overlayer; indeed, it is well established that such remote polar – also referred to as interface phonons – may play an important role in determining the electrical and optical properties of heterojunction devices [4]–[7]. We compute the effective mobility of 2DEG limited by carrier scattering with surface acoustic phonons and remote polar phonons. We have used the conduction band offset $\Delta E_c = 1.7$ V [3] at the interface.

Manuscript received November 21, 2021; accepted December 2, 2021. Date of publication December 6, 2021; date of current version December 29, 2021. This work was supported in part by ARL-ARO Award W911NF1920086. The review of this letter was arranged by Editor V. Moroz. *(Corresponding author: Ramji Singh.)*

The authors are with the Department of Electrical and Computer Engineering, University of Illinois at Chicago, Chicago, IL 60607 USA (e-mail: rsingh54@uic.edu).

Color versions of one or more figures in this letter are available at https://doi.org/10.1109/LED.2021.3132894.

Digital Object Identifier 10.1109/LED.2021.3132894

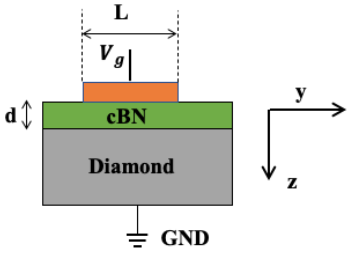

Fig. 1. The model cBN/Diamond FET. The cBN/Diamond interface is contained in the xy plane. The gate metal layer (orange) with an area $S = L^2$ forms a Schottky contact with the cBN layer. The diamond substrate thickness is taken to be 100 nm for calculations.

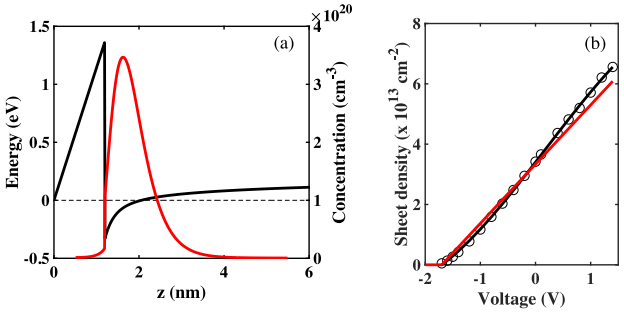

Fig. 2. **(a)** Conduction band profile (black) with $\Delta E_C = 1.7$V and the corresponding volume charge density (n) at no gate bias. The dashed lined shows the Fermi level. **(b)** The red curve shows the sheet charge density predicted by gauss law $n_s = \frac{\varepsilon_0 \varepsilon_{c\text{-}BN}(0)}{q(d+\Delta d)}(V_g - V_{th})$ for average 2DEG thickness of 0.80 nm ($\varepsilon_{c\text{-}BN}(0) = 7.1$ [16]). Δd attains a maximum value of 1.2 nm at -0.4 V and decreases to 0.36 nm at 1.4 V. The black curve shows the actual sheet density obtained by integrating volume charge density in (1) w.r.t z from $z = 1.2$nm to $z = 6$ nm. The threshold voltage $V_{th} = \Phi_B - \Delta E_c = -1.7$ V.

II. The Two-Dimensional Electron Gas

We use the 1D Schrödinger Poisson simulator [8], [9] to simulate the heterostructure consisting of undoped cubic Boron Nitride (cBN) as the top overlayer over the undoped diamond substrate (Fig. 1). We find that for cBN thickness, $1.1 \leq d \leq 1.8$ nm the ground state energy of the electron below Fermi level. For our analysis we take $d = 1.2$ nm.

The electrons at the cBN/Diamond interface are confined by triangular potential well whose slope is modulated by the applied gate bias, V_g (Fig. 2(a)). Presently, there is no experimental data available on the surface density of states and

Fermi level pinning for cBN. For simplicity we have assumed a 0 eV Schottky barrier (Φ_B) at the gate metal/cBN interface, we would like to point out that the inclusion of Schottky barrier height will only change the threshold voltage (the minimum applied gate voltage required to produce 2DEG).

For a total p bound states in the triangular well the volume density of electrons is given as:

$$n(z) = k_B T \frac{m^*}{\pi \hbar^2} \sum_{i=1}^{p} |\psi_i(z)|^2 \, log\left(1 + e^{\frac{E_F - E_i}{k_B T}}\right) \quad (1)$$

where, m^* is the effective mass of electron, E_i is the i^{th} energy eigen value of electron, T is the absolute temperature, k_B is the Boltzmann's constant and E_F is Fermi level. The Fig. 2(a) shows the volume density as a function of position z. For the present case we find 9 bound states out of which the ground state is 14.7 meV below the Fermi level. The first excited state is approximately 5.3 k_BT above the Fermi level for which the probability of occupancy less than 0.5% and hence all the states except the ground states are empty. The electrons confined by the triangular well are thus confined to the ground state but behave as plane waves in the plane which contains the cBN/Diamond interface. The electrons in the ground state subband interact with phonons to scatter from a momentum eigenstate $|\,k\rangle$ to $|\,k'\rangle$ where, k is the wavevector in the plane containing the cBN/Diamond interface.

The 2DEG sheet density (n_s) results from the contribution of ground state electrons only. The applied gate voltage (V_g) modulates the slope of the triangular well causing the ground eigenstate to move further down below the Fermi level and the higher excited states move further upwards if the voltage is increased from 0V, accordingly the sheet density increases. The contribution of higher states to sheet density negligible.

We determine the thickness of 2DEG at a given gate bias as:

$$\Delta d = \frac{\text{Area under the volume charge density}}{\text{peak value of volume charge density } (n_{peak})} \quad (2)$$

III. Electron-Phonon Interaction

A. Description of Remote Polar Phonon

The presence of cBN/Diamond heterointerface causes localization of longitudinal optical (LO) phonons in cBN layer (medium 1) which appear as evanescent modes leaking into the underlying diamond layer (medium 2). These modes can be expressed as linear combination of symmetric and anti-symmetric components with the Fröhlich Hamiltonian as [10], [11]:

$$H^{A/S} = \sum_q g(\omega, q) \frac{1}{\sqrt{2q}} e^{iq\cdot\rho} \left(a_q + a_{-q}^{\dagger}\right) e^{-q\left(z - \frac{d}{2}\right)} \quad (3)$$

where,

$$g(\omega, q) = \left[\frac{4\pi\hbar e^2 S^{-1}}{\varepsilon_d^2 \left(\partial/\partial\omega\right)\left(\varepsilon_1(\omega) f(qd/2) + \varepsilon_2(\omega)\right)}\right]^{1/2} \quad (4)$$

and, $f(qd/2) \equiv \tanh\left(\frac{qd}{2}\right)$ or $\coth\left(\frac{qd}{2}\right)$ for symmetric and anti-symmetric modes, respectively.

In (4), q is the phonon wavevector, d is the cBN thickness, $S = L^2$ is the area of heterointerface, ε_d is the static dielectric constant of diamond ($\varepsilon_d = 5.7$ [14]), ω is the phonon frequency obtained by the solution of the following secular equation for each mode:

$$\varepsilon_1(\omega) f(qd/2) + \varepsilon_2(\omega) = 0 \quad (5)$$

B. Remote Polar Phonon Scattering

To obtain the analytical expression of scattering rate of electrons in the ground state subband, we model the ground state wavefunction by Fang-Howard approximation [12], [13]:

$$\psi(r) = \sqrt{\frac{b^3}{2}} (z - l) e^{-\frac{b}{2}(z-l)} \frac{e^{-i\boldsymbol{k}\cdot\boldsymbol{r}_\parallel}}{\sqrt{S}} \quad (6)$$

where, 'b' is a variational parameter, $b = \sqrt[3]{\frac{48\pi m e^2 n_s}{\varepsilon_d \varepsilon_0 \hbar^2}}$ [12], (n_s is numerically estimated as shown in Fig 2(b)), $m = 0.57 m_0$ [15] the electron effective mass for diamond, ε_0 is the vacuum permittivity and $r_\parallel$ is the position vector in the x-y plane and l is the depth of 2DEG from the interface.

The scattering rate given by the Fermi's golden rule [11]:

$$\frac{1}{\tau^{\{e,a\}}} = \frac{S}{(2\pi)^2} \int d^2\mathbf{q} \left(\frac{2\pi}{\hbar}\right) |M(q)|^2 \, \delta\left(E_{\mathbf{k}'} - E_{\mathbf{k}} \pm \hbar\omega\right) \quad (7)$$

In (7) the upper (plus) sign corresponds to emission and the lower (minus) sign corresponds to absorption (also the superscripts e and a corresponds to emission and absorption), we will adhere to this convention throughout the letter.

Here, $|M(q)|$ is the electron-phonon coupling matrix element given as:

$$|M(q)| = \left\langle k', N_q \pm \frac{1}{2} \pm \frac{1}{2} \middle| H^{A/S} \middle| k, N_q \pm \frac{1}{2} \mp \frac{1}{2} \right\rangle \quad (8)$$

where, $N_q = 1/\left(\exp\left(\frac{\hbar\omega}{k_B T}\right) - 1\right)$ is the phonon occupation number. Accordingly, (7) becomes:

$$\frac{1}{\tau_{S,A}^{\{e,a\}}} = \frac{b^6 S}{2\pi} \frac{m}{\hbar^3 k} \int_{q=q_1}^{q=q_2} dq \frac{g^2(\omega, q)}{q} \frac{1}{\sqrt{\left|1 - \left(\frac{q}{2k} \pm \frac{m\omega}{\hbar k q}\right)^2\right|}} \quad (9)$$

where, the limits of integration are determined by:

$$-1 \le \left(\frac{q}{2k} \pm \frac{m\omega}{\hbar k q}\right) \le 1 \quad (10)$$

In (10), ω is substituted from (5) to obtain the limits on q.

Now, we express the scattering rate due to emission/absorption by symmetric and anti-symmetric mode as below:

$$\frac{1}{\tau^{\{e,a\}}} = \frac{1}{\tau_{sym}^{\{e,a\}}} + \frac{1}{\tau_{Anti-sym}^{\{e,a\}}} \quad (11)$$

and the total scattering rate is given by:

$$\frac{1}{\tau^{tot}} = \frac{1}{\tau^{e}} + \frac{1}{\tau^{a}} \quad (12)$$

The emission/absorption rates are plotted in Fig. 3(a). The mobility of electron is expressed as:

$$\mu_{op} = \frac{e < \tau_{Tot} >}{m^*} \quad (13)$$

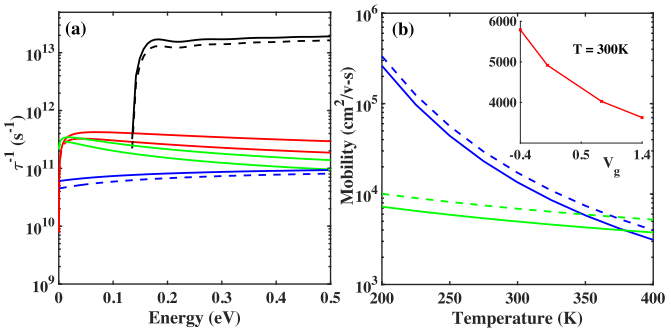

Fig. 3. **(a)** Phonon scattering rate: Emission rate for remote polar phonon (black) and surface acoustic phonon (red); Absorption rate for remote polar phonon (blue) and surface acoustic phonon (green) **(b)** Mobility versus temperature for remote polar phonon (blue) and surface acoustic phonon (green) [Inset fig: effective mobility μ_0 (in cm^2/v-s) at various gate voltage at room temperature]. (The solid lines indicate gate voltage +1.4 V and dashed line indicates 0V).

C. Scattering by Surface Acoustic Phonon

The presence of interface modifies the bulk acoustic waves as Rayleigh waves, which are elliptically polarized waves localized near the interface with a velocity $V_R = \omega/q$ along the interface, interacts with the carrier through deformation potential resulting from distortion of the lattice causing local changes in the crystal energy bands. The particle displacement in the second quantized form is given as [13]:

$$\hat{U}(r) = \sqrt{\frac{\hbar}{2\rho\omega S}}u(r)\left(a_q + a^{\dagger}_{-q}\right) \tag{14}$$

The deformation- potential interaction Hamiltonian is given as:

$$H_{def} = E_a \sum_q \nabla \cdot \hat{U}(r)$$
$$= -E_a \frac{\omega^2}{V_l^2}\sqrt{\frac{\hbar}{2\rho\omega S}}\sum_q u(z)\left(a_q e^{iq\cdot r_\parallel} + a^{\dagger}_{-q}e^{-iq\cdot r_\parallel}\right) \tag{15}$$

where, $\nabla.u(r) = -\left(\frac{\omega^2}{V_l^2}\right)u(z)\,e^{iq\cdot r_\parallel}$; $u(z) = Ae^{-\alpha_{tl}z}; r_\parallel$ is the position vector in xy plane; $A^2 = \frac{A_2}{q} = \frac{2s^2n/(n-s)^2}{q\left(1+s^2n/(n-s)\right)}$, $n = \sqrt{1-\frac{V_R^2}{V_l^2}}$ and $s = \sqrt{1-\frac{V_R^2}{V_s^2}}$, E_a is the electron deformation potential (8.7eV [15]), α_{tl} is the imaginary part of the transverse wavevector of longitudinal acoustic wave, ρ is the density of diamond (3.51 gm/cm^3 [15]), V_l/V_s is the longitudinal/shear acoustic velocity ($18.21 \times 10^5/12.3 \times 10^5$ cm/sec [15]) and $V_R = 11.21 \times 10^5$ cm/sec [15].

The scattering rate is obtained from (7), (8) and (15) as below [13]:

$$\frac{1}{\tau^{\{e,a\}}} = \frac{m^* E_a^2 V_R^3 A_2}{\pi\hbar^2 k\rho V_l^4}\int_{q=q_1}^{q=q_2} dq \frac{b^6 e^{-2\alpha_{tl}l}}{(\alpha_{tl}+b)^6} \times \frac{q^2}{\sqrt{\left|1-\left(\frac{q}{2k}\pm\frac{m^*V_R}{\hbar k}\right)^2\right|}}\left(N_q + \frac{1}{2}\pm\frac{1}{2}\right) \tag{16}$$

where, l is the depth of 2DEG from the interface. The limits of integration depends on threshold energy of electron [13], $E_{th} = \frac{m^*V_R^2}{2} = 0.2038$ meV. The limits for emission (upper sign) and absorption (lower sign) respectively for electron energy $E \geq E_{th}$ is:

$$q_1 = 0 \quad \text{and } q_2 = 2k\left(1 \mp \frac{m^*V_R}{\hbar k}\right) \tag{17}$$

No emission occurs for electron energy, $E \leq E_{th}$, whereas the limits for absorption for is:

$$q_1 = 2k\left(-1+\frac{m^*V_R}{\hbar k}\right) \quad \text{and } q_2 = 2k\left(1+\frac{m^*V_R}{\hbar k}\right) \tag{18}$$

The effective mobility due to combined effect of remote polar phonon (μ_{op}) and surface acoustic phonon (μ_{ac}) can be represented as:

$$\frac{1}{\mu_0} = \frac{1}{\mu_{ac}} + \frac{1}{\mu_{op}} \tag{19}$$

IV. Discussion

The absorption rate of surface acoustic phonon is about an order of magnitude higher than the remote polar phonon at low energies which gradually decreases and become comparable for energies greater than 0.4 eV (Fig 3(a)).

The emission threshold for remote polar phonons is 0.154 eV, whereas, for surface acoustic phonons it is 0.2038 meV. The emission rate is on average 60 times higher for remote polar phonon than surface acoustic at 1.4V gate bias which increases to 80 times at 0 V showing higher sensitivity of acoustic phonon to electron sheet density.

From (9) and (16), it is evident that for a given energy of electron the maximum contribution to scattering is obtained from long wavelength phonons, with this approximation we can estimate that, the scattering rate expression shows a quadratic $\sim n_s^2$ variation with the 2DEG sheet density. Hence, the mobility varies as $\sim n_s^{-2}$ as is evident form Fig 3(b) (inset).

V. Conclusion

In this letter we investigated the conditions for the formation of a 2DEG at cBN-diamond interface and found that the surface density obtained is on the order of 10^{13} cm^{-2}. At room temperature for the gate voltage increasing from 0 to +1.4V, the mean free time of electron due to remote polar phonon varies from 5.57 ps to 4.36 ps whereas for Rayleigh phonon it varies from 2.23 ps to 1.61ps, consequently the mobility limited by remote polar phonon is approximately $\sim$ 2.5 times higher than Rayleigh wave (Fig. 3(b)). This result is significant because it implies that the surface acoustic phonon (Rayleigh waves) is the dominant scattering mechanism and the existence of the remote polar phonon effect does not have a major detrimental effect of the mobility. In particular, the surface acoustic phonon scattering dominates over remote polar phonon scattering for temperatures below 375 K.

Acknowledgment

The authors are grateful for enlightening interactions with Michael Spencer, Michael Shur, Tony Ivanov, Mahesh R. Neupane, and A. Glen Birdwel.

REFERENCES

[1] M. Kasu, N. C. Saha, T. Oishi, and S.-W. Kim, "Fabrication of diamond modulation-doped FETs by NO_2 delta doping in an Al_2O_3 gate layer," *Appl. Phys. Exp.*, vol. 14, no. 5, May 2021, Art. no. 051004, doi: 10.35848/1882-0786/abf445.

[2] J. Shammas, Y. Yang, X. Wang, F. A. M. Koeck, M. R. McCartney, D. J. Smith, and R. J. Nemanich, "Band offsets of epitaxial cubic boron nitride deposited on polycrystalline diamond via plasma-enhanced chemical vapor deposition," *Appl. Phys. Lett.*, vol. 111, no. 17, Oct. 2017, Art. no. 171604, doi: 10.1063/1.5009089.

[3] N. Narendra, J. Narayan, and K. W. Kim, "Diamond/c-BN HEMTs for power applications: A theoretical feasibility analysis," 2019, *arXiv:1901.10572*.

[4] K. Hess and P. Vogl, "Remote polar phonon scattering in silicon inversion layers," *Solid State Commun.*, vol. 30, no. 12, pp. 797–799, Jun. 1979.

[5] B. T. Moore and D. K. Ferry, "Remote polar phonon scattering in Si inversion layers," *J. Appl. Phys.*, vol. 51, no. 5, p. 2603, 1980.

[6] G. Bonomo, A. Mohamed, S. Farid, K. Park, M. Dutta, and M. A. Stroscio, "Contribution of remote interface polar phonons in the hole mobility of diamond," *Diamond Rel. Mater.*, vol. 101, Jan. 2020, Art. no. 107650.

[7] M. A. Stroscio, M. Kisin, G. Belenky, and S. Luryi, "Phonon enhanced inverse population in asymmetric double quantum wells," *Appl. Phys. Lett.*, vol. 75, no. 21, pp. 3258–3260, Nov. 1999.

[8] I. Tan, G. L. Snider, L. D. Chang, and E. L. Hu, "A self-consistent solution of Schrödinger–Poisson equations using a nonuniform mesh," *J. Appl. Phys.*, vol. 68, no. 8, pp. 4071–4076, Oct. 1990, doi: 10.1063/1.346245.

[9] *1D Poisson Program*. Accessed: Mar. 3, 2021. [Online]. Available: https://www3.nd.edu/~gsnider/

[10] K. W. Kim and M. A. Stroscio, "Electron-optical-phonon interaction in binary/ternary heterostructures," *J. Appl. Phys.*, vol. 68, no. 12, pp. 6289–6292, Dec. 1990, doi: 10.1063/1.346871.

[11] M. A. Stroscio and M. Dutta, *Phonons in Nanostructures*. Cambridge, U.K.: Cambridge Univ. Press, 2001.

[12] T. Ando, B. Alan Fowler, and F. Stern, "Electronic properties of two-dimensional systems," *Rev. Mod. Phys.*, vol. 54, p. 437, Apr. 1982, doi: 10.1103/RevModPhys.54.437.

[13] R. Singh, G. Bonomo, S. Farid, M. R. Neupane, A. G. Birdwell, T. G. Ivanov, M. Dutta, and M. A. Stroscio, "Surface-acoustics phonon scattering in 2D-hole gas of diamond based FET devices," *Carbon*, vol. 169, pp. 488–500, Nov. 2020, doi: 10.1016/j.carbon.2020.07.078.

[14] L. Reggiani, D. Waechter, and S. Zukotynski, "Hall-coefficient factor and inverse valence-band parameters of holes in natural diamond," *Phys. Rev. B, Condens. Matter*, vol. 28, no. 6, 1983, pp. 3550–3555, doi: 10.1103/PhysRevB.28.3550.

[15] F. Nava, C. Canali, C. Jacoboni, L. Reggiani, and S. F. Kozlov, "Electron effective masses and lattice scattering in natural diamond," *Solid State Commun.*, vol. 33, no. 4, 1980, pp. 475–477, doi: 10.1016/0038-1098(80)90447-0.

[16] K. Karch and F. Bechstedt, "Ab initiolattice dynamics of BN and AlN: Covalent versus ionic forces," *Phys. Rev. B, Condens. Matter*, vol. 56, no. 12, pp. 7404–7415, Sep. 1997, doi: 10.1103/PhysRevB.56.7404.